

Hammad Farooq

Effect of CuCl and Zn on Cu₃Si Formation and Coke Deposition in the Direct Synthesis of Dimethyldichlorosilane

In collaboration with Elkem

August 2020



Norwegian University of
Science and Technology

Effect of CuCl and Zn on Cu_3Si Formation and Coke Deposition in the Direct Synthesis of Dimethyldichlorosilane

In collaboration with Elkem

Hammad Farooq

Chemical Engineering

Submission date: August 2020

Supervisor: Hilde Johnsen Venvik, IKP

Co-supervisor: Edd Anders Blekkan, IKP
Mehdi Mahmoodinia, IKP

Norwegian University of Science and Technology
Department of Chemical Engineering

Preface

The thesis has been completed in the Department of Chemical Engineering at the Norwegian University of Science and Technology (NTNU), in collaboration with Elkem Silicone Materials. The thesis work was accomplished under the supervision of Professor Hilde J. Venvik and co-supervision of Professor Edd A. Blekkan and Dr. Mehdi Mahmoodinia at the Department of Chemical Engineering at NTNU, Trondheim. The thesis report was submitted to NTNU.

Acknowledgment

Foremost, I would like to express my sincere gratitude to my supervisor, Professor Hilde J. Venvik, for providing valuable guidance and support throughout the thesis work. Her feedback in the weekly discussions and support during the COVID-19 pandemic has been of immense help. I would also like to thank my co-supervisor, Professor Edd A. Blekkan, for his feedback during the meetings.

I extend my heartfelt gratitude to my co-supervisor, Dr. Mehdi Mahmoodinia, for his continuous guidance throughout the semester. His enthusiasm for research and work ethics are a great source of inspiration for me.

My appreciation also extends to Torbjørn Røe and Harry Rong from Elkem Silicone Materials for helpful discussions and suggestions.

I would like to thank senior engineer Estelle M. Vanhaecke and senior advisor Anne Hoff for providing technical training and support during the laboratory work.

Last but not least, I am eternally grateful to my parents for motivating me. Without their encouragement, support, and inspiration, I would have never been able to come this far. I would also like to thank my friends and family for the motivation they have given me throughout my studies.

Abstract

The direct synthesis of dimethyldichlorosilane has been studied for more than 60 years, owing to its significance in the silicones industry. The direct process is a reaction of distinct complexity because of silicon taking part in the catalytic cycle and forming Cu_3Si and $\text{Cu}_{15}\text{Si}_4$ alloy phases, where Cu_3Si is the catalytically active intermediate. In addition, the side reactions and cracking of chloromethane during the direct reaction lead to coke formation on the active surface. In spite of its importance, the role of CuCl and Zn on the coke formation, Cu_3Si formation, and its transformation to $\text{Cu}_{15}\text{Si}_4$ phase is not entirely understood. A series of reacted contact mass samples with varying reaction time and amount of CuCl and Zn was characterized by using x-ray diffraction (XRD) to study the phase transformation. Raman spectroscopy and thermogravimetric analysis (TGA) coupled with mass spectrometry (MS) were utilized to investigate the structural order and reactivity of coke, respectively.

XRD analyses of samples with CuCl and Zn indicated that the standard amount of CuCl and Zn limited the enrichment of inactive copper and $\text{Cu}_{15}\text{Si}_4$ formation, while five times the amount of CuCl and Zn caused high enrichment of inactive copper. Samples without the addition of Zn exhibited a high tendency of $\text{Cu}_{15}\text{Si}_4$ and inactive copper formation. In addition, the investigation on the structural order of deposited coke by using Raman spectroscopy revealed that the addition of Zn changes the coke to a more ordered graphitic carbon, as the reaction proceeds. TGA analyses pointed out that coke in all the reacted contact mass samples starts to oxidize at around $200\text{ }^\circ\text{C}$. In Zn -promoted samples, the CO_2

mass spectrum peak became more distinct and narrower with an increase in reaction time. While in samples without Zn, the CO₂ signal was noticed to be broad with a shoulder peak at a higher temperature of 340 °C. It was found that Zn-promoted samples had slightly more reactive coke.

Table of Contents

PREFACE	I
ACKNOWLEDGMENT	I
ABSTRACT	III
LIST OF FIGURES.....	VII
LIST OF TABLES	X
LIST OF ABBREVIATIONS AND SYMBOLS.....	XI
1 INTRODUCTION	1
1.1 SCOPE OF THE THESIS	3
2 THEORY	5
2.2 THE COMPLEXITY OF THE DIRECT SYNTHESIS	5
2.3 ROLE OF THE CU-BASED CATALYST	6
2.4 ROLE OF THE Cu_3Si ACTIVE PHASE	7
2.5 ROLE OF ZN AND SN AS PROMOTERS	8
2.6 CATALYST DEACTIVATION BY COKE FORMATION.....	10
2.6.1 Coke Formation in the Direct Synthesis.....	11
2.7 CHARACTERIZATION TECHNIQUES.....	13
2.7.2 Powder X-ray Diffraction (XRD).....	13
2.7.3 Raman Spectroscopy	15
2.7.4 Thermogravimetric Analysis (TGA)	17
2.7.5 Differential Scanning Calorimetry (DSC).....	18
3 MATERIALS AND METHODS.....	19
3.1 CATALYST AND CONTACT MASS SAMPLES.....	19
3.2 X-RAY DIFFRACTION (XRD)	21
3.3 RAMAN SPECTROSCOPY.....	21
3.4 THERMAL ANALYSIS	22

4	RESULTS AND DISCUSSION.....	23
4.1	CHARACTERIZATION OF SI, CUCL AND CUCL/SI MIXTURE	23
4.2	EFFECT OF CUCL AND ZN ON THE ACTIVE PHASE FORMATION.....	32
4.3	SURFACE ANALYSIS TO STUDY ORDER OF COKE	37
4.3.6	Fluorescence in the Raman spectra.....	37
4.3.7	Inhomogeneous Surface Distribution.....	39
4.3.8	Phase Chemistry of Coke.....	41
4.4	EFFECT OF ZN ON THE REACTIVITY OF COKE.....	48
4.4.9	Samples with Zn	48
4.4.10	Samples without Zn	56
4.4.11	Comparison of Coke Reactivity	62
5	CONCLUSION.....	67
6	FUTURE WORK.....	69
	BIBLIOGRAPHY.....	71
	APPENDIX A.....	89
A.1	RAMAN SPECTROSCOPY RESULTS	89
A.2	THERMAL ANALYSIS RESULTS.....	91
	APPENDIX B.....	103
B.1	RISK ASSESSMENT	103

List of Figures

Figure 2.1: Diffraction of x-rays by atoms in a periodic lattice.....	14
Figure 2.2: Rayleigh scattering and Raman scattering illustration.	16
Figure 4.1: XRD spectrum of Si-Ref sample	24
Figure 4.2: XRD spectra of S0-URCM, and CuCl.....	24
Figure 4.3: TGA and DSC results of Si-Ref sample.....	26
Figure 4.4: TGA and DSC results for CuCl in oxidative atmosphere.	27
Figure 4.5: TGA and DSC results for CuCl in inert atmosphere	27
Figure 4.6: TGA and DSC results of unreacted contact mass sample, S0-URCM	28
Figure 4.7: Raman spectra for pure silicon, Si-Ref, and unreacted contact mass sample, S0.....	31
Figure 4.8: XRD spectra of S11, S12, S13 and S14	32
Figure 4.9: XRD spectra of S15, S16, S17 and S18	33
Figure 4.10: XRD spectra of S19 and S20	33
Figure 4.11: Raman spectrum of S16.....	38
Figure 4.12: Raman spectrum of S11 at two different spots.....	39
Figure 4.13: Raman spectra of S11, S15, S12 and S16 samples.....	42
Figure 4.14: Raman spectra of S13, S17, S19, S14, S18 and S20 samples.	42
Figure 4.15: Raman spectra of reacted contact mass samples.	44

Figure 4.16: TGA, DSC and MS analysis of S11 in oxidative atmosphere	50
Figure 4.17: TGA, DSC and MS analysis of S15 in oxidative atmosphere	51
Figure 4.18: TGA, DSC and MS analysis of S17 in oxidative atmosphere	54
Figure 4.19: TGA, DSC and MS analysis of S19 in oxidative atmosphere	55
Figure 4.20: TGA, DSC and MS analysis of S12 in oxidative atmosphere	58
Figure 4.21: TGA, DSC and MS analysis of S16 in oxidative atmosphere	59
Figure 4.22: TGA, DSC and MS analysis of S18 in oxidative atmosphere	60
Figure 4.23: TGA, DSC and MS analysis of S20 in oxidative atmosphere	61
Figure 4.24: Raman spectra of S19 at the same spot.....	65
Figure A.1: Raman spectra of Si-Ref, S0, S11, S13 and S16.....	89
Figure A.2: Microscope image of S19 sample showing coke oxidation under Raman laser.....	90
Figure A.3: Mass spectroscopic analysis of Si-Ref sample in oxidative atmosphere	91
Figure A.4: Mass spectroscopic analysis of CuCl sample in oxidative atmosphere	91

Figure A.5: Mass spectroscopic analysis of CuCl sample in inert atmosphere	92
Figure A.6: Mass spectroscopic analysis of S0 sample in oxidative atmosphere	92
Figure A.7: TGA, DSC and MS analysis of S0 in inert atmosphere ..	93
Figure A.8: TGA, DSC and MS analysis of S11 in inert atmosphere	94
Figure A.9: TGA, DSC and MS analysis of S15 in inert atmosphere	95
Figure A.10: TGA, DSC and MS of S17 in inert atmosphere	96
Figure A.11: TGA, DSC and MS analysis of S19 in inert atmosphere	97
Figure A.12: TGA, DSC and MS analysis of S12 in inert atmosphere	98
Figure A.13: TGA, DSC and MS analysis of S16 in inert atmosphere	99
Figure A.14: TGA/MS analysis of S18 in inert atmosphere.....	100
Figure A.15: TGA, DSC and MS analysis of S20 in inert atmosphere	101
Figure A.16: Mass spectrometry result of NaHCO ₃ in oxidative atmosphere	102

List of Tables

Table 3.1: CuCl, pure silicon, fresh contact mass, and reacted contact mass.....	20
Table 4.1: FWHM of and G band. ID/IG ratios.....	46
Table 4.2: Temperature profile of CO ₂ formation and H/C ratios.....	63

List of Abbreviations and Symbols

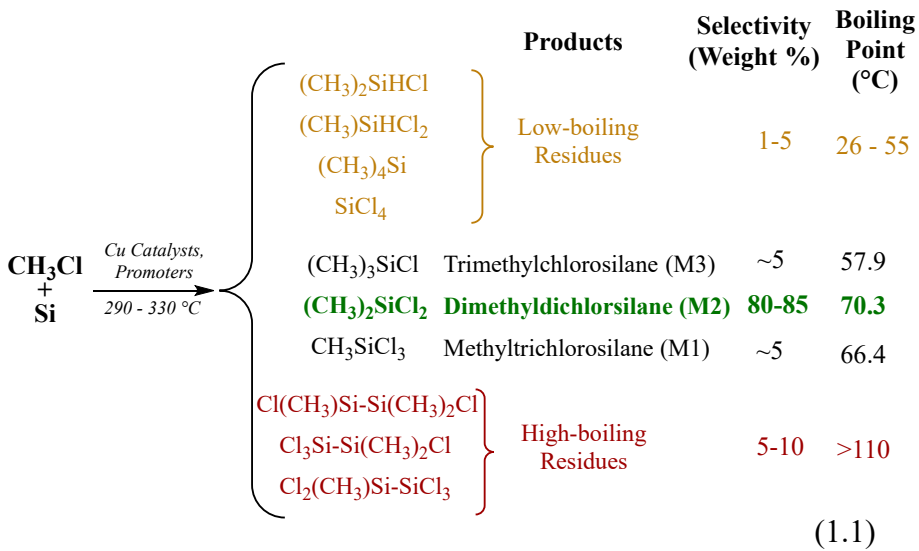
Abbreviations	Explanation
a.u.	Arbitrary units
DSC	Differential scanning calorimetry
EDS	Energy-dispersive spectroscopy
FWHM	Full width at half maximum
ICDD	International Centre for Diffraction Data
ID/IG	The ratio of D-band intensity to G-band intensity
GC	Gas chromatography
H/C	Hydrogen to carbon ratio
MCS	Methylchlorosilanes
M2	Dimethyldichlorosilane
MS	Mass spectrometry
PDF	Powder Diffraction File
RF	Response factor
S(T)EM	Scanning (transmission) electron microscopy
TGA	Thermogravimetric analysis
TPO	Temperature-programmed oxidation
XRD	X-ray diffraction

Symbols	Explanation
θ	Diffraction angle of the incident beam to the reflected beam
λ	Wavelength
λ	Lattice number
ν_0	Frequency of incident beam
ν_m	Frequency of molecular vibrations

1 Introduction

The direct synthesis of dimethyldichlorosilane (M2), commonly referred to as the Rochow reaction, was first discovered by Eugene G. Rochow and formed the basis of the modern silicone production, a several billion-dollar per year industry [1]–[3]. Dimethyldichlorosilane (M2) is the most desired monomer in the industrial-scale production of silicones [4]–[6]. Silicones are high-performance synthetic polymers containing repeating Si-O backbone units, where organic groups are attached to the silicon via a silicon-carbon bond [7]. The importance of dimethyldichlorosilane (M2) is highlighted by the crucial role of silicones in our society. Silicones are used in the medical industry, automotive industry, and cosmetic industry [3]. Silicones are extensively used in the automotive industry owing to their water resistance and electrically insulating properties [3]. Silicones are now being employed in the medical industry as they are compatible with human tissue [8].

The direct synthesis is a heterogeneous catalytic process, whereby a solid mixture of a Cu-based catalyst, silicon (Si) and selected promoters, referred to as the contact mass, reacts with gaseous chloromethane to produce a wide range of products [9]. It is believed that the significant discovery of Rochow was the use of the copper catalyst. Equation 1.1 shows the direct process of dimethyldichlorosilane (M2) and the formation of by-products [2], [5], [10]. Dimethyldichlorosilane (M2), the most desired product out of a variety of compounds formed, is produced with 80-90 % selectivity [11].



The direct synthesis of dimethyldichlorosilane is a unique and complicated process, as it is a gas (CH_3Cl) – solid (Si) – solid (Cu catalyst) reaction [12]. This gas-solid-solid reaction is affected by several factors, including reaction time, reaction temperature, type of reactor, complex component interactions, and a number of products produced [12], [13]. The reaction between silicon and Cu-based catalyst, in the direct reaction, is also influenced by mixing, grinding, and proportion of these two phases, as well as the thickness of the SiO_2 layer on silicon [14]. Furthermore, the main reactant, silicon, plays a role in the catalytic process and forms the active Cu_3Si alloy phase [15].

Like many other catalytic processes, the Rochow reaction is also a victim of catalyst deactivation due to the formation of coke on the surface of the active solid phase [16]. The coke formation occurs due to the cracking of chloromethane at localized hotspots formed in the direct process [17]. The nature of formed coke is not completely understood;

however, it is established that the nature of the coke formed is controlled by active solid phase, reaction conditions, preparation of the contact mass, catalyst properties, and the type of the reactor [14]. The direct synthesis of dimethyldichlorosilane has been studied extensively over the years, and several mechanisms have been proposed [18]–[20]. Bažant proposed that the high selectivity towards dimethyldichlorosilane in the direct process might be due to the formation of an active intermetallic compound, Cu_3Si [20].

1.1 Scope of the Thesis

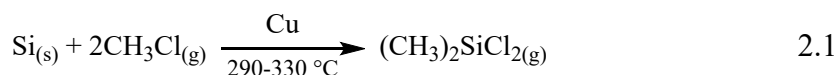
In spite of the extensive research on the direct synthesis of dimethyldichlorosilane, the role of promoters and catalyst on the formation of Cu_3Si alloy phase and its transformation to other copper silicide phases is not entirely understood [10]. Furthermore, there is no consensus among the researcher on the mechanism behind the catalyst deactivation due to coke formation [10]. In order to understand the mechanism behind catalyst deactivation by coke formation, it is first essential to investigate the type of coke by analyzing its structural order, and reactivity. Relevant analytical techniques have been employed and optimized to better understand the nature of the contact mass sample, and the formation of coke and Cu_3Si alloy phase. In this work, copper-based catalyst, unreacted contact mass, and reacted contact mass samples are analyzed by utilizing a number of characterization techniques. The results are discussed in relation to the previously reported studies.

2 Theory

2.2 The complexity of the Direct Synthesis

The copper-catalyzed direct synthesis of dimethyldichlorosilane (M2) has been studied for more than 60 years, but the exact reaction mechanism and role of the catalyst is still not clear [21]. The direct process is the only gas-solid-solid catalytic reaction at an industrial scale [22]–[24].

When the contact mass, a mixture of Si, Cu-based catalyst, and promoters come in contact with the CH₃Cl gas at a temperature of 290–330 °C, the production of M2 takes place, as shown in Equation 2.1 [25]. As detailed by Equation 1.1, a number of other products and by-products are formed along with dimethyldichlorosilane. Selectivity towards the most desirable product, dimethyldichlorosilane (M2), is affected by the selection of Cu-based catalyst, promoters, and impurities present in the silicon [22], [26].



The interface between copper and silicon is so complicated that silicon itself takes part in the catalytic cycle [15]. Zhang *et al.* reported that copper is not the main active catalytic phase but reacts with silicon to form an active intermediate Cu-Si alloy, Cu₃Si [10]. In a fluidized bed reactor, the Rochow reaction comes to a halt before all the silicon is consumed due to the deactivation of the active phase by coke deposition

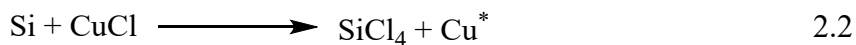
and enrichment of inactive copper on the surface [26]. All of the discussed factors in the Rochow reaction, i.e., the role of the catalyst, the role of the active phase, selection of promoters, and catalyst deactivation due to coke formation, make it a particularly complicated process.

2.3 Role of the Cu-based Catalyst

The direct synthesis of dimethyldichlorosilane became possible due to the use of metallic copper as a catalyst by Rochow and Müller [18]. Hurd and Rochow reported that the reaction of pure silicon with chloromethane, without the addition of copper, results in a very minute yield of methylchlorosilanes [18]. Ever since, various compounds of copper have been studied as a catalyst in the Müller-Rochow process [10]. These compounds of copper, also called coppers, are not the active catalysts themselves, but rather the catalyst precursors as they ultimately transform to an active phase [10]. However, the term “catalyst” and “catalyst precursor” are often used interchangeably in the Rochow reaction [10].

In the past decade, CuCl has been extensively studied as a catalyst in the Rochow reaction due to its ability to increase reaction activity and decrease the induction period [27]. The induction period is a universal term in the Rochow reaction and is defined as the time period when the active catalytic surface is formed [28]–[30]. Silicon conversion and selectivity towards M2 is affected by CuCl morphology, particle size, route of synthesis, composition, and structure [25]. The emphasis on the morphology of the CuCl catalyst has been reported previously [12]. It was reported by Chen *et al.* that CuCl crystals with the dendritic

structure and exposed (1 1 1), (2 0 0), and (2 2 0) planes demonstrate higher silicon conversion and selectivity toward dimethyldichlorosilane than irregularly structured CuCl [12]. Acker et al. showed that CuCl prepared by wet chemical method exhibits higher reactivity than industrial-bought dry process CuCl [14]. Equation 2.2 shows a generalized reaction between CuCl and Si in the direct synthesis [25].



The activated Cu^* diffuses to the bulk of silicon to form the active copper-silicide phases [25].

2.4 Role of the Cu_3Si Active Phase

In the Rochow reaction, the catalytic ability of copper evolves due to being able to form binary intermetallic compounds [31]. Trambouze *et al.* reported that Cu_3Si , known as η -phase, is the active intermetallic specie and acts as the active catalytic phase in the Rochow reaction [32]. The reaction progresses by continuous consumption of Si from Cu_3Si alloy, and the free Cu^* again diffuses into the bulk Si to form new Cu_3Si species [33]–[36]. It was reported that the concentration of η -phase decreases while the amount of metallic copper increases with the reaction time [32]. On the contrary, Krylov *et al.* proposed that η -phase acts as a reservoir for free copper [37]. This was, however, debunked by Voorhoeve, who confirmed that Cu_3Si was found to be present in all the reacted contact masses [31].

Falconer *et al.* suggested that Cu_3Si provides an active surface for selective dimethyldichlorosilane formation, but it is not the only copper silicide phase present in the reacted contact mass [23], [38]. Another intermetallic compound $\text{Cu}_{15}\text{Si}_4$, called ϵ -phase, has also been discovered in the reaction [38]. Luo *et al.* showed that the formation of $\text{Cu}_{15}\text{Si}_4$ depends on the CuCl particle size [38]. Agglomeration of CuCl particles leads to the formation of $\text{Cu}_{15}\text{Si}_4$ [38]. $\text{Cu}_{15}\text{Si}_4$ acts as a continuous reservoir for the catalytic η -phase, but the reactivity is decreased due to this decomposition step of $\text{Cu}_{15}\text{Si}_4$ to Cu_3Si [38].

2.5 Role of Zn and Sn as Promoters

A promoter is a material which, when added to a reaction in a small quantity, increases the performance of the catalyst [39]. Promoter itself has no significant catalytic ability but interacts with the active catalytic phase to enhance the reaction activity [40]. Wessel *et al.* studied the role of zinc (Zn) and tin (Sn) as promoters in the Rochow reaction by formulating the contact mass mixture with 88.98 wt.% Si, 10 wt.% Cu, 1 wt.% Zn, and 0.02 wt.% Sn composition [41]. It was reported that Zn decreases the enrichment of inactive metallic copper by efficiently dispersing the copper on the silicon surface [41].

Ward *et al.* found that Zn and Sn, when added together, show a synergistic effect [2]. Sn, when added alone, has no effect on the reactivity and selectivity [2]. It was reported that the addition of Zn and Sn, in small quantity, increases the selectivity towards M2 by hindering coke formation [42]. Zn inhibits the deposition of coke by acting as a

methylating agent, and its methylating power is improved by the addition of Sn [42].

The promoting ability of Zn and Sn is highly dependent on their respective concentrations [36]. These promoters, when added in amounts of more than 1 wt.%, have an adverse effect on M2 selectivity [43]. Wang *et al.* also reported that the addition of Zn in CuCl-Si contact mass increases the formation of Cu₃Si alloy, while the addition of Sn increases the consumption of the active Cu₃Si [36].

2.6 Catalyst Deactivation by Coke Formation

Catalyst deactivation, described as degradation of catalytic activity and selectivity over time, is an inescapable process [44], [45]. There are different modes of catalyst deactivation, such as catalyst poisoning due to chemisorption of species on catalytic sites, thermal degradation due to loss of surface area, vapor formation by reaction of gaseous phase with catalyst, and coke formation where deposition of carbonaceous species on the active catalytic sites hinders the reaction [45]. Both terms, “coke” and “carbon” are used interchangeably, as the difference between carbon and coke is somewhat arbitrary [39]. Bartholomew described coke as a product of the decomposition of hydrocarbons and carbon as a product of carbon monoxide (CO) disproportionation [44].

Deactivation of a catalyst by coke formation is a pervasive occurrence in reactions involving hydrocarbons [46], [47]. The structural order of the coke formed depends on the properties of the catalyst and reaction conditions [48]. It is reported that the surface structure of catalytic sites, such as the pore structure of the catalyst, affects the formation of C-C bonds during coke formation [45].

Properties of coke, such as hydrogen to carbon ratio (H/C), reactivity, and oxidation temperature, depend on certain conditions of formation [45]–[47]. At reaction temperatures below 200 °C, coke is formed mainly due to vapor condensation and has a relatively high hydrogen-to-carbon (H/C) ratio [49]. This type of coke is referred to as white coke and mainly consists of polyolefins [39], [45]. Coke formed at a temperature above 200 °C consists of polyaromatic condensed-ring structures and features an H/C value of 0.5 or less [39], [47]. Nature of

carbonaceous species formed at a reaction temperature of 800 °C and above mirrors the properties and structure of graphitic carbon [50]. Such type of coke has essentially no hydrogen contents and is highly ordered [39].

2.6.1 Coke Formation in the Direct Synthesis

The mechanism behind catalyst deactivation by coke formation is the least understood area of the Rochow reaction [41]. As discussed in section 2.6, the formation of coke is dependent on the reaction conditions and type of catalyst. Side reactions during the direct process result in the coke formation on the active catalytic sites [20]. Clarke reported that carbon deposited on the surface is the result of the cracking of chloromethane on copper [27]. An empirical description of coke formation is shown in Equation 2.3 [27].



Bažant *et al.* proposed that the coke deposited on the active sites due to decomposition of methyl radicals may consist of polymethylenes [20]. Wessel and Rethwisch studied the effect of Zn promoter on the formation of Coke [41]. It was reported that there are two types of cokes formed on the surface; α -coke, which does not affect the catalytic activity, and β -coke, which is formed on top of the active sites and is responsible for the degradation in the activity [41]. β -coke was found to have a higher oxidation temperature than the α -coke [41]. The deposition of coke on the active sites results in the enrichment of inactive copper

[38]. In order to understand the mechanism behind catalyst deactivation by coke formation, it is first essential to investigate the type of coke by analyzing its structural order, and reactivity. The analytical techniques utilized for this purpose are discussed in the following section.

2.7 Characterization Techniques

Characterization techniques relevant to the investigation of the role of catalyst and promoter on the active phase formation and coke deposition are studied in this section. X-ray diffraction (XRD) is a commonly used tool to study the crystalline structure of a material and phase transformations. Thermogravimetric analysis (TGA) and Raman spectroscopy are utilized to analyze the properties of the deposited coke.

2.7.2 Powder X-ray Diffraction (XRD)

Being a non-destructive and relatively fast method, powder x-ray diffraction (XRD) is the most frequently applied characterization technique, usually used to recognize the presence of different crystalline phases in the powder material and their structure [39]. When a metallic anode is bombarded with high energy electrons, radiations of specific wavelengths are emitted. The properties of the emitted radiations depend on the selection of the metallic anode. In powder XRD, the usual standard is to use Cu-K α radiations from copper anode [39]. Cu-K α ($\lambda=1.54 \text{ \AA}$) lines are emitted when a primary electron creates a hole in the K shell, which is then filled from the L shell [51]. The energy of Cu-K α lines is sufficient to penetrate solid material, and the wavelength is almost the same order of magnitude as the inter-atomic distances [52].

In a crystalline solid, the diffraction of incoming x-rays occurs due to the elastic scattering of x-rays photons by planes of periodically spaced atoms [51]. The diffracted x-rays, which are in phase, lead to constructive interference. The condition of the constructive interference is governed by Bragg's law, given in equation 2.4, where λ is the

wavelength of x-rays, d is the interatomic distance, and θ is the incident angle of x-rays [51], [53].

$$n\lambda = 2d\sin\theta \quad (n = 1,2,3, \dots) \quad 2.4$$

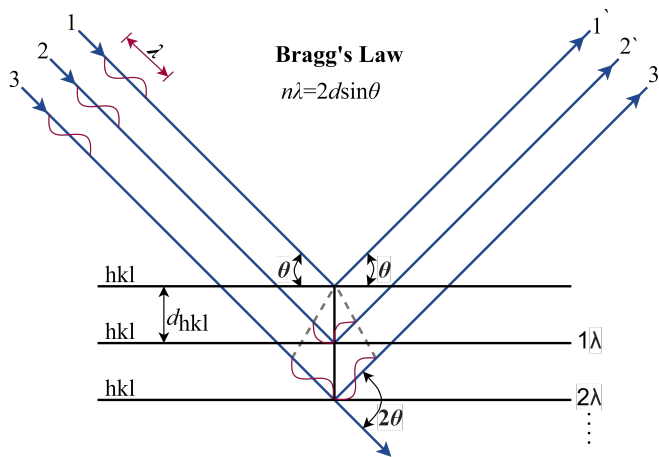


Figure 2.1: Diffraction of x-rays by atoms in a periodic lattice, governed by Bragg's law. Reproduced from reference [53].

In a crystalline powder sample, the constructive interference occurs, as there will always be a crystal plan direction which is positioned at a right angle with the incident beam. The width of the diffracted peak can also provide information about the crystallite size, D , as explained by the Scherrer formula in equation 2.5 [39].

$$\text{FWHM} = \frac{K\lambda \times 57.3}{D \cos\theta} \quad 2.5$$

In Scherrer formula, K is a constant related to the crystalline shape and can be taken as one, θ is the incident angle, λ is the wavelength of x-rays, and FWHM is the full width at half-maximum of a diffracted peak.

2.7.3 Raman Spectroscopy

Raman spectroscopy falls under the category of vibrational spectroscopy techniques. It is based on the principle that when a material is irradiated with a monochromatic light such as a laser, the electromagnetic radiations will get scattered by the molecules of that material [54], [55]. If the frequency of the photons of electromagnetic radiations (ν_0) is the same as the molecular vibrations (ν_m), the molecule will get excited to a higher virtual energy state. Upon de-excitation, the scattering of the radiations will either be elastic, i.e., the scattered light has the same frequency as the incident light ($\nu_0 = \nu_m$) or inelastic, i.e., the scattered photons have a higher or lower frequency than that of the incident photons ($\nu_0 \pm \nu_m$). Elastic scattering is known as Rayleigh scattering, and the inelastic scattering is the Raman scattering.

Figure 2.2 illustrates the Rayleigh and Raman scattering [56]. In Raman scattering, if the final energy level of the molecules is higher than the initial state ($\nu_0 + \nu_m$), it is called Stokes scattering [54]. If the final energy of the molecular vibrations is lower than that of the initial state ($\nu_0 - \nu_m$), then this is referred to as the anti-Stokes scattering [57]. The signal intensity of Stokes scattering is considerably higher than that of the anti-Stokes scattering; thus, a Raman spectrometer calculates frequency changes produced by the Stokes scattering. In Rayleigh scattering, the molecule rises to a higher virtual energy state but quickly

falls back to its initial ground state, without any energy change. The scattered photon, thus, has the same frequency as the incident light [54].

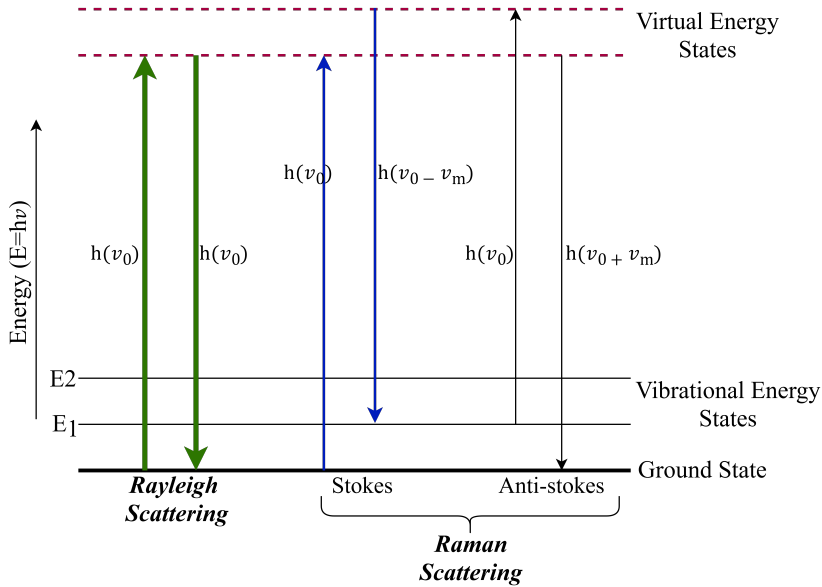


Figure 2.2: Rayleigh scattering and Raman scattering illustration. Raman scattering consists of Stokes and anti-Stokes lines. The thickness of each line represents the signal intensity. Reproduced from reference [56].

The phenomenon of Raman scattering was first discovered by Sir C.V. Raman [58]. This characterization technique can provide effective information about the changes in the composition of a material. In cases where the use of XRD is not applicable, such as when the material has an amorphous phase, Raman spectroscopy becomes even more practical. Analysis of the Raman spectrum of powder material is complicated due to the variable particle size and inhomogeneous particle distribution [39]. The vibrations modes that can be detected by Raman spectroscopy technique are referred to as Raman active modes.

2.7.4 Thermogravimetric Analysis (TGA)

Thermogravimetric analysis (TGA) is a temperature-programmed characterization technique utilized to determine the change in the sample mass, while the temperature is raised at a linear rate [59]. The temperature range of TGA instruments is more than 1200 °C, and it can analyze mass change caused by drying, oxidation, reduction, and decomposition [60]. The atmosphere in the TGA analysis can be set to oxidative, reductive, or inert. In an oxidative atmosphere, either air or pure oxygen is pumped to the instrument's chamber, while in an inert atmosphere, usually helium or argon is fed to the instrument [60]. TGA analysis requires a minimal amount of sample in the range of a few milligrams. It is possible to perform TGA with a post-analysis instrument such as a gas chromatography instrument (GC) or a mass spectrometer (MS), which can provide an insight to the reaction mechanism and mass conservative changes. The TGA results are analyzed by plotting the mass change with respect to temperature or time. Another valuable representation is the use of derivative thermogravimetry (DTG) which can pinpoint the rate of mass change at a specific temperature value [61].

This characterization technique is sensitive to several parameters, such as the heating rate, process enthalpy, electrostatic forces, and electronic drift [60]. Sudden changes in the heating rate, usually caused by the variations in the gas flow, can give rise to apparent mass increase or mass loss. This is attributed to the buoyancy effect [61]. The buoyancy effect is caused by the decrease in the density of the surrounding gas in the TGA chamber. This usually occurs at initial temperatures when the gas flow is turned on and causes an apparent increase in mass [61]. To

minimize the buoyancy effect, it is recommended to keep the gas flow the same throughout the experiment.

2.7.5 Differential Scanning Calorimetry (DSC)

Differential scanning calorimetry (DSC) is a widely used thermal analysis technique and applied to measure thermal changes in a sample as a function of temperature [62]. DSC is usually coupled with temperature-programmed techniques, such as TGA [63]. DSC works by examining the difference in the thermal changes of sample material with that of a reference sample [62]. This indirect and “differential” method is employed because there is no method that can directly measure the heat flow in and out of a sample [64]. Based on the method of determining the thermal events in the sample, there are two types of DSC systems: the heat-flux DSC, which measures the heat flow difference based on the temperature difference, and power-compensated DSC which works by measuring the enthalpy change of the sample [65].

In power-compensated DSC, a material sample and reference sample are placed on a separate heating element, and the temperature difference is always kept zero ($\Delta T=0$) [65]. When a thermal change occurs in the material sample, the power to the heating element is also changed in order to keep the temperature difference to zero [65]. This power change is plotted either as an exothermic peak or an endothermic peak. An endothermic event occurs when positive power input is required, and an upward peak is noticed. On the other hand, in an exothermic event, the compensated power is observed as a downward peak.

3 Materials and Methods

3.1 Catalyst and Contact Mass Samples

The metallurgical grade silicon, CuCl catalyst and contact mass samples were provided by Elkem Silicon Materials. Unreacted contact mass mixture, denoted as S0-URCM, contains a standard amount of CuCl catalyst, Zn as a promoter, and Sn as a promoter. Reacted contact mass samples were reacted in a fluidized bed reactor for a defined amount of time without any subsequent addition. The reactor was run at 4 bar and 300 °C, while chloromethane and argon gases were fed at a rate of 285 mL/min and 10 mL/min, respectively.

Samples S11 and S15 are promoted with a standard amount of both promoters, Zn and Sn, and have a reaction time of 5 and 16 hours, respectively. In contrast, S12 and S16 are only promoted with a standard amount of Sn and have a reaction time of 5 and 16 hours, respectively.

S13, S17, and S19, samples with five times the amount of catalyst, Zn, and Sn, have a reaction time of 5, 16, and 40 hours, respectively. S14, S18, and S20 were reacted for 5, 16, and 40 hours, respectively, with five times the amount of catalyst and Sn, but without the addition of Zn.

Table 3.1 summarizes the explanation of the analyzed samples. The classification of the reacted contact mass samples is carried out based on the reaction time and relative amount of Zn.

Table 3.1: CuCl, pure silicon, fresh contact mass, and reacted contact mass samples with an explanation of the added species.

Sample	Explanation	CuCl amount	Zn amount	Sn amount
CuCl	Pure CuCl	-	-	-
Si-Ref	MG silicon	-	-	-
S0	S0-URCM	Standard	Standard	Standard
S11	S11-CuZnSnSi-5h	Standard	Standard	Standard
S12	S12-CuSnSi-5h	Standard	-	Standard
S13	S13-Si5(CuZnSn)-5h	5 times	5 times	5 times
S14	S14-Si5(CuSn)-5h	5 times	-	5 times
S15	S15-CuZnSnSi-16h	Standard	Standard	Standard
S16	S16-CuSnSi-16h	Standard	-	Standard
S17	S17-Si5(CuZnSn)-16h	5 times	5 times	5 times
S18	S18-Si5(CuSn)-16h	5 times	-	5 times
S19	S19-Si5(CuZnSn)-40h	5 times	5 times	5 times
S20	S20-Si5(CuSn)-40h	5 times	-	5 times

MG: Metallurgical grade. URCM: Unreacted contact mass

3.2 X-ray Diffraction (XRD)

X-ray diffraction was carried out with the DaVinci1 diffractometer, which employs Cu K α radiation ($\lambda=1.54060 \text{ \AA}$) from the copper anode. The optimized results were obtained when using a total scan time of 60 minutes. A 15 mm cavity sample holder was found to provide good results while utilizing less quantity of the powder sample. For each sample, a continuous scan from a 2θ range of 15° to 80° was run. The obtained raw files were analyzed with Bruker AXS DIFFRACT.EVA (v5.1) to strip the Cu K α peaks from the spectrum. The stripped data was then matched with the powder diffraction database (PDF) by The International Centre for Diffraction Data (ICDD).

3.3 Raman Spectroscopy

Horiba Jobin Yvon LabRAM HR800 spectrometer, operated by LabSpec 6 Spectroscopy Suite software, was used to measure the Raman spectrum of the samples. The instrument was configured to use 632 nm Ne-Ne laser, x50LWD objective, and 600 gr/mm grating in a range of 200 cm^{-1} - 1800 cm^{-1} . A built-in microscope with x50 objective lens was used to focus the laser onto the selected spot. The fluorescence effect was minimized by de-focusing the laser and optimizing the acquisition and accumulation parameters for each sample measurement. The instrument was configured to run in multi-accumulation mode to avoid the peaks caused by cosmic rays.

3.4 Thermal Analysis

Thermogravimetric analysis (TGA), differential scanning calorimetry (DSC), and mass spectrometry (MS) of samples were performed on Netzsch STA 449C Jupiter TGA/DSC instrument coupled with Netzsch Aëolos QMS 403C Mass Spectrometer. For each measurement, the temperature profile was set at a heating rate of 10 °C/min from the initial temperature to 800 °C. Analysis in the oxidative atmosphere was carried out with the gas flow set at 25 mL/min of argon and 55 mL/min of air (20% O₂ 80% N₂). The experiments in an inert atmosphere were carried out with the gas flow set at 80 mL/min of argon. It is noteworthy that exothermic peaks in the DSC curve are plotted downwards.

Before starting the measurement, each sample was kept in the TGA chamber for 30 minutes at stand-by while the gas flow was turned on. This was done to achieve an isothermal environment and consequently to minimize the buoyancy effect. The buoyancy effect causes an apparent mass increase at the initial temperature if the temperature difference between the sample and the environment is too high.

4 Results and Discussion

Contact mass samples with varying amount of CuCl, Zn and reaction time have been thoroughly characterized to investigate the crystalline phase structure of pure silicon and CuCl, formation of surface complexes, the evolution of Cu₃Si and Cu₁₅Si₄ alloy phases, silicon oxidation, degree of the structural order of carbonaceous material, and reactivity of the deposited coke.

4.1 Characterization of Si, CuCl and CuCl/Si mixture

Figure 4.1 shows the XRD spectrum of the pure silicon sample, Si-Ref. Figure 4.2 shows the XRD spectra of CuCl and unreacted contact mass sample, S0. XRD spectra in both figures are measured from the 2θ value of 15° to 80° . The XRD diffractogram of Si-Ref, presented in Figure 4.1, shows five characteristic peaks of silicon at 2θ values of 28.5° , 47.3° , 56.1° , 69.1° , and 76.4° [4], [66]. The standard XRD pattern of silicon (ICDD 00-027-1402), also plotted in Figure 4.1, shows that these peaks belong to (1 1 1), (2 2 0), (3 1 1), (4 0 0), and (3 3 1) planes of silicon, respectively.

In Figure 4.2, the standard XRD pattern of CuCl (ICDD 04-007-2951) pinpoints the CuCl diffraction peaks at 2θ values of 28.5° , 33° , 47.4° , 56.2° , 69.2° and 76° , which belong to (1 1 1), (2 0 0), (2 2 0), (3 1 1), (4 0 0), and (3 3 1) planes, respectively.

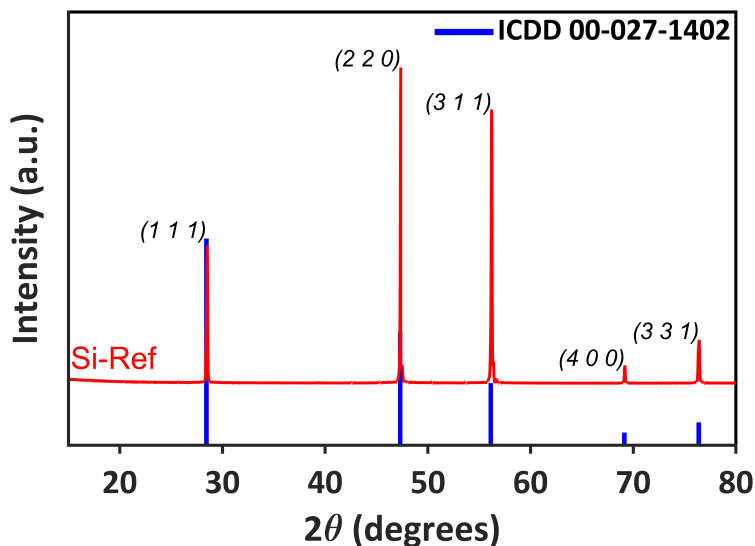


Figure 4.1: XRD spectrum of Si-Ref sample. Measured in 2θ range of 15° to 80° . Standard silicon PDF card is plotted.

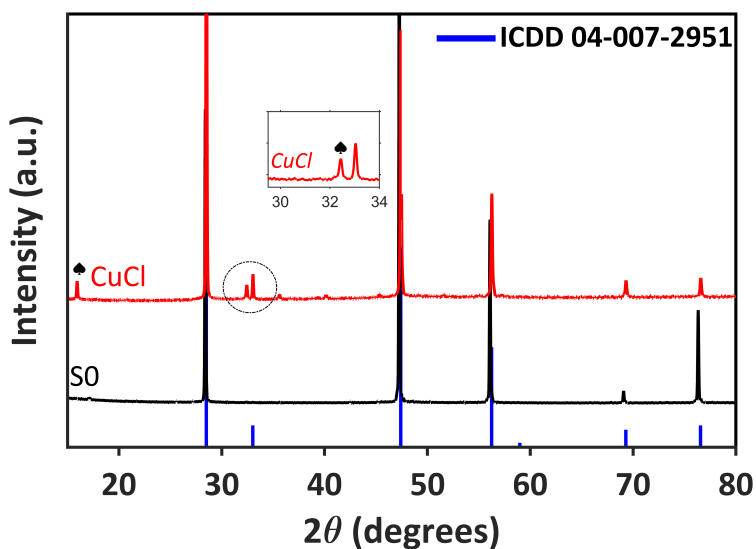
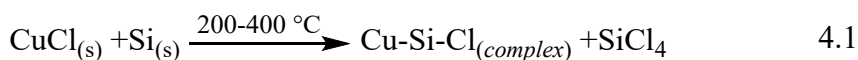


Figure 4.2: XRD spectra of S0-URCM, and CuCl. Measured in 2θ range of 15° to 80° . ♠ shows CuCl_2 peaks. Standard CuCl PDF card is plotted.

An enhanced CuCl spectrum from 2θ value of 30° to 34° 2θ is also presented in Figure 4.2, which shows the presence of copper(II) chloride (CuCl_2) in the CuCl sample. The first peak in the enhanced plot, at 32.47° 2θ , has been reported to belong to (2 2 0) plane of CuCl_2 [67], [68]. The peak at around 16° in the CuCl spectrum also shows the presence of CuCl_2 and belongs to (0 0 1) plane [69], [70]. Pure CuCl is white, but the visible observation of the CuCl sample indicated a greenish color, which is introduced due to the presence of CuCl_2 [71].

It is immediately observed that all the characteristic peaks of CuCl other than the relatively weaker peak at 33.03° , are positioned at the same 2θ values as those of silicon. Wang *et al.* also pointed out this overlapping of silicon and CuCl peaks when studying the structure of CuCl/Si mixture for the Rochow reaction [72]. This phenomenon makes it harder to identify the presence of CuCl in the reacted or unreacted contact mass samples with the help of XRD analysis. The XRD spectrum of unreacted contact mass sample S0, in Figure 4.2, shows five major diffraction peaks at the same 2θ values as those for pure silicon (Figure 4.1). These peaks are the combined effect of silicon and CuCl. The weaker peak at 33.03° 2θ in the CuCl spectrum is not detected in the XRD spectrum of sample S0. In the Rochow reaction, the reaction between silicon and CuCl begins with the formation of the surface Cu-Si-Cl complexes, as shown in Equation 4.1 [72].



Thermogravimetric analysis (TGA) and differential scanning calorimetry (DSC) result for Si-Ref in the oxidative atmosphere is shown in Figure 4.3. The mass change curve for Si-Ref reveals that the sample undergoes an initial mass loss of 1.35 %, from the initial temperature to 100 °C, due to drying of the absorbed moisture [73]. From 100 °C and onwards, oxidation of silicon over the whole temperature range is noticed. It has previously been reported that the oxidation of silicon occurs at both lower and higher temperatures [74]. Wessel *et al.* reported that this continuous oxidation of silicon happens in the reacted contact mass samples as well, and makes it difficult to draw a baseline in the TGA curve [41].

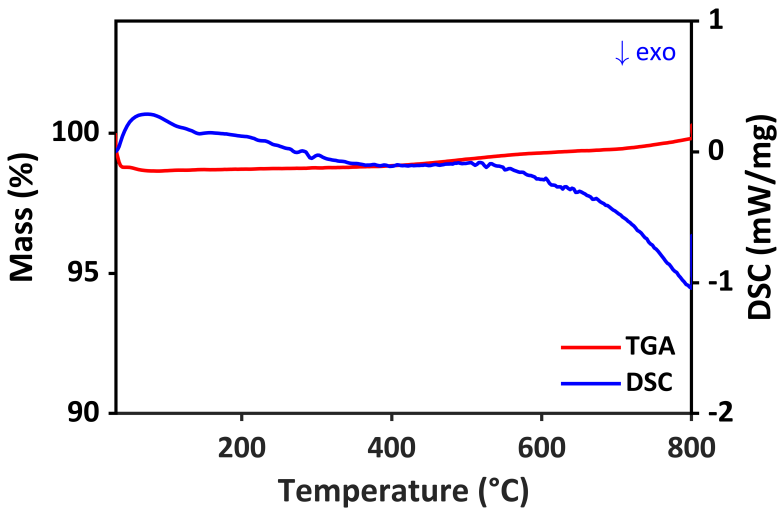


Figure 4.3: TGA and DSC results of Si-Ref sample in an oxidative atmosphere (55 ml/min air and 25 ml/min argon). Measured from 35 °C to 800 °C at a heating rate of 10 K/min.

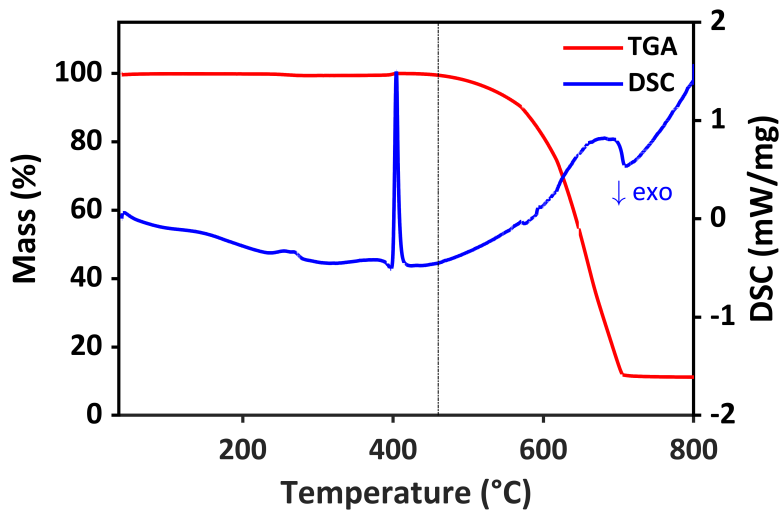


Figure 4.4: TGA and DSC results for CuCl in an oxidative atmosphere (55 ml/min air and 25 ml/min argon). Measured from 35 °C to 800 °C at a heating rate of 10 K/min.

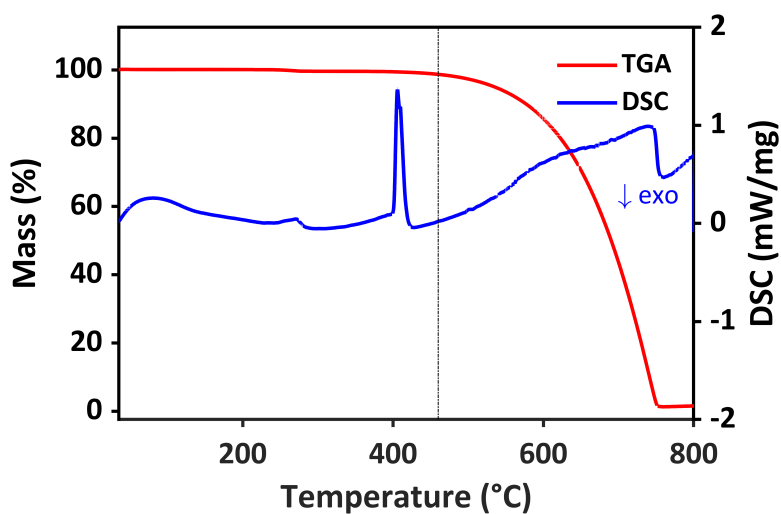


Figure 4.5: TGA and DSC results for CuCl in an inert atmosphere (80 ml/min argon). Measured from 35 °C to 800 °C at a heating rate of 10 K/min.

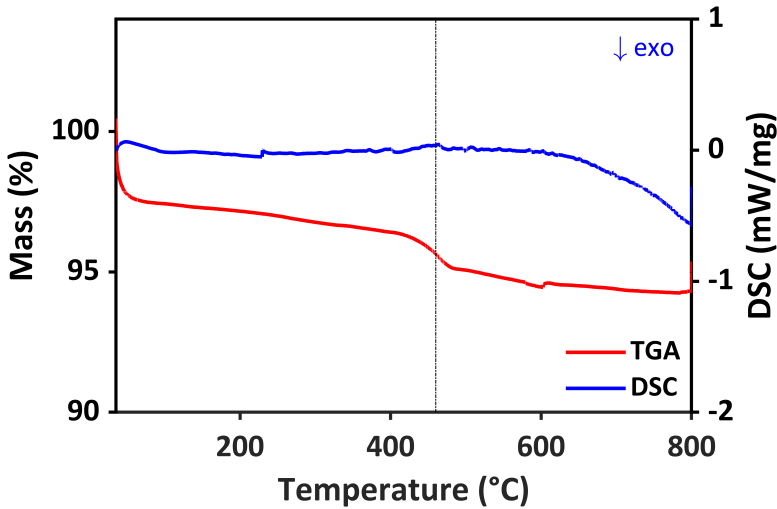
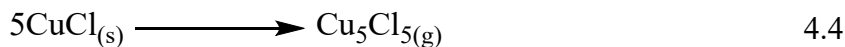
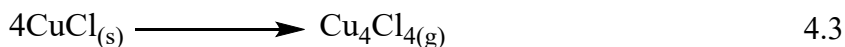
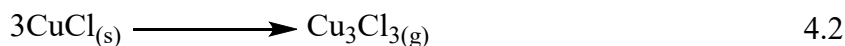


Figure 4.6: TGA and DSC results of unreacted contact mass sample, S0-URCM, in an oxidative atmosphere (55 ml/min air and 25 ml/min argon). Measured from 35 °C to 800 °C at a heating rate of 10 K/min.

Figure 4.4 and Figure 4.5 show the TGA/DSC analysis of the CuCl sample, in an oxidative and inert atmosphere, respectively. Below 100 °C, CuCl does not experience any significant mass loss in both atmospheres. From 400 °C to 800 °C, CuCl goes through a mass loss of 88 % in the oxidative environment, as shown in Figure 4.4, and a mass loss of 98 % in an inert environment, as shown in Figure 4.5. The melting point of CuCl is reported to be around 422 °C [75]. Above this temperature, CuCl is dissociated into vapor phase $\text{Cu}_3\text{Cl}_3(\text{g})$, $\text{Cu}_4\text{Cl}_4(\text{g})$, and $\text{Cu}_5\text{Cl}_5(\text{g})$ in the following manner [76].



Multiple attempts to obtain the MS spectra for Cu_xCl_x ($x=3,4,5$) were conducted using the procedure reported by Guido *et al.*, but due to the upper mass-to-charge ratio of the available mass spectrometer instrument, none were successful [76]. Figure A.4 and Figure A.5 show the mass spectrometry results for CuCl in an oxidative and inert atmosphere, respectively.

Figure 4.6 shows the TGA/DSC results for the unreacted contact mass sample, S0, in an oxidative atmosphere. Below 100 °C, sample S0 undergoes a mass loss of around 2.5 % due to the drying process. Figure A.6 shows the mass spectrometry (MS) ion current signal for water ($m/z=18$) below 100 °C for sample S0, in an oxidative atmosphere.

Unlike Si-Ref in Figure 4.3, sample S0 in Figure 4.6 experiences a continuous mass loss after 100 °C, which becomes quite sharp at around 422 °C, the melting point of CuCl [75]. This mass loss can be attributed to the decomposition of catalyst precursor, CuCl, as described in Figure 4.4. Similar behavior is noticed for the S0 sample in inert TGA measurement, shown in Figure A.7. It should be noted that the mass change in Figure 4.6 for sample S0 is a combined effect of the mass increase due to silicon oxidation and mass decrease due to CuCl decomposition.

Figure 4.7 shows the Raman spectra of Si-Ref, and unreacted contact mass sample, S0, from the Raman shift value of 200 cm^{-1} to 1400 cm^{-1} . Both spectra are offset along the y-axis by an arbitrary value and have also been cut at a random value of the highest peak at 519 cm^{-1} for clarity.

Five major peaks at Raman shift values of 300 cm^{-1} , 430 cm^{-1} , 519 cm^{-1} , 615 cm^{-1} , and 940 cm^{-1} in the Raman spectra of both samples belong to unique phononic modes of pure silicon. Uchinokura *et al.* pointed out that these peaks are related to the Raman spectrum of silicon, while the tallest peak at around 519 cm^{-1} is the one-phonon silicon peak [77]. Graczykowski *et al.* reported that the peaks at 300 cm^{-1} and 430 cm^{-1} are attributed to the 2TA phononic mode of silicon [78]. Peaks at 520 cm^{-1} and 940 cm^{-1} were reported to belong to LO and 2TO phononic modes of silicon, respectively [78]. The peak at 615 cm^{-1} could either belong to the TO or TA phononic modes [78]. Here TA implies transverse acoustic, TO is short for transverse optic, and LO stands for longitudinal optic [78].

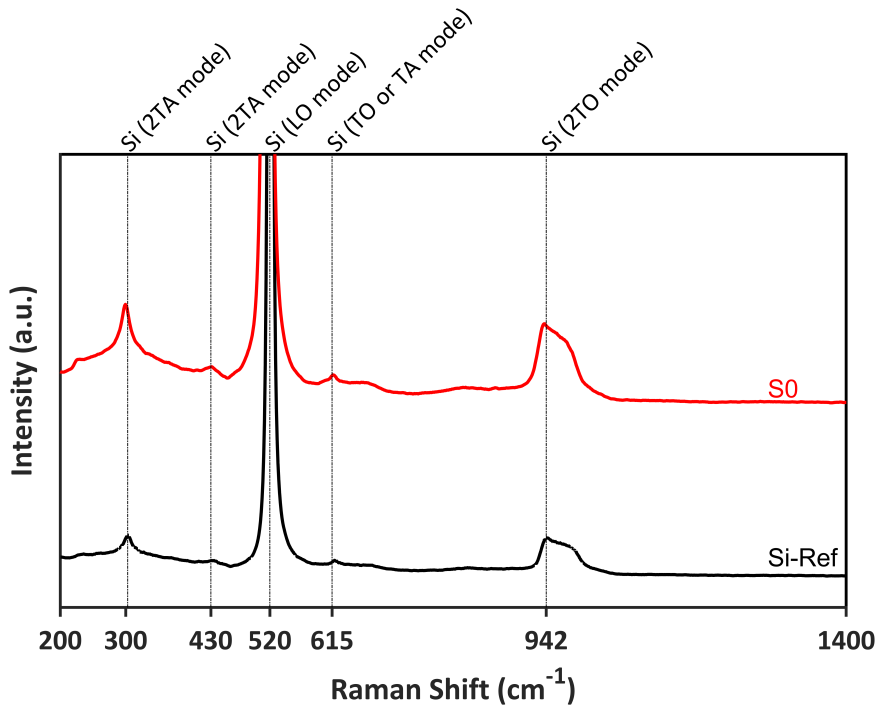


Figure 4.7: Raman spectra for pure silicon, Si-Ref, and unreacted contact mass sample, S0. Measured from Raman shift value of 200 cm⁻¹ to 1400 cm⁻¹ in visible light with 632 nm laser. Both spectra are offset along y-axis for clarity.

The peaks at around 300 cm⁻¹ and 615 cm⁻¹ show a relatively high intensity in sample S0. This could be due to the contribution of oxides of copper, which show the Raman peaks at around 293 cm⁻¹ and 623 cm⁻¹ [79].

4.2 Effect of CuCl and Zn on the Active Phase Formation

Cu_3Si is known to be the active catalytic phase in the Rochow reaction [72]. Wang *et al.* reported that the presence of the Cu_3Si in the contact mass represents the potential activity [36]. Effect of Zn on the Cu_3Si formation and its phase transformation is studied by analyzing samples from S11 to S20 with x-ray diffraction (XRD).

Figure 4.8(a), Figure 4.9(a), and Figure 4.10(a) show the XRD spectra for samples S11 to S14 (5 hours reaction time), S15 to S18 (16 hours reaction time), and S19-S20 (40 hours reaction time), respectively. All the diffractograms in the mentioned figures are analyzed from the 2θ value of 15° to 80° . Enlarged views between 2θ values of 42° and 46° are presented in Figure 4.8(b), Figure 4.9(b), and Figure 4.10(b), which correspond to samples S11 to S14, S15 to S18, and S19-S20, respectively. For clarity and comparison, each spectrum has been offset along the y-axis by an arbitrary value.

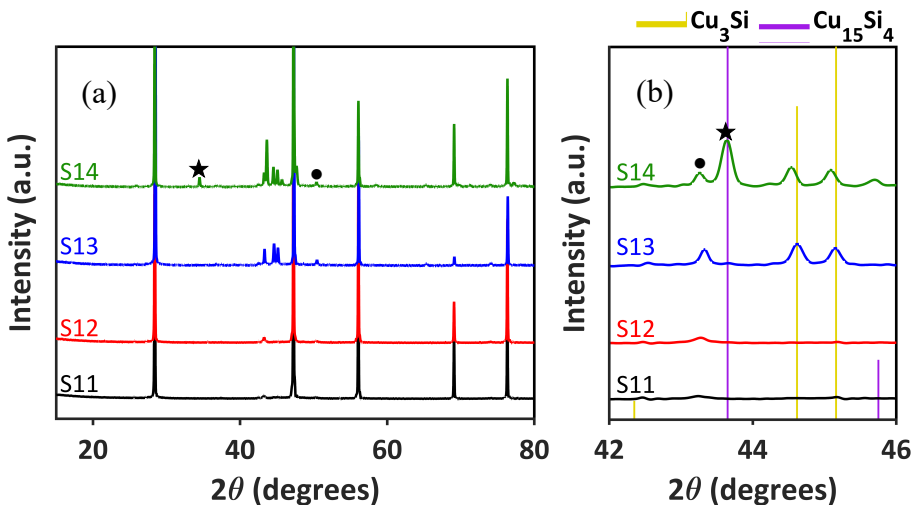


Figure 4.8: XRD spectra of S11, S12, S13 and S14. (a) 2θ range of 15° to 80° . \star shows $\text{Cu}_{15}\text{Si}_4$. \bullet shows metallic Cu (b) 2θ range of 42° to 46° . Standard PDF for Cu_3Si and $\text{Cu}_{15}\text{Si}_4$ are plotted.

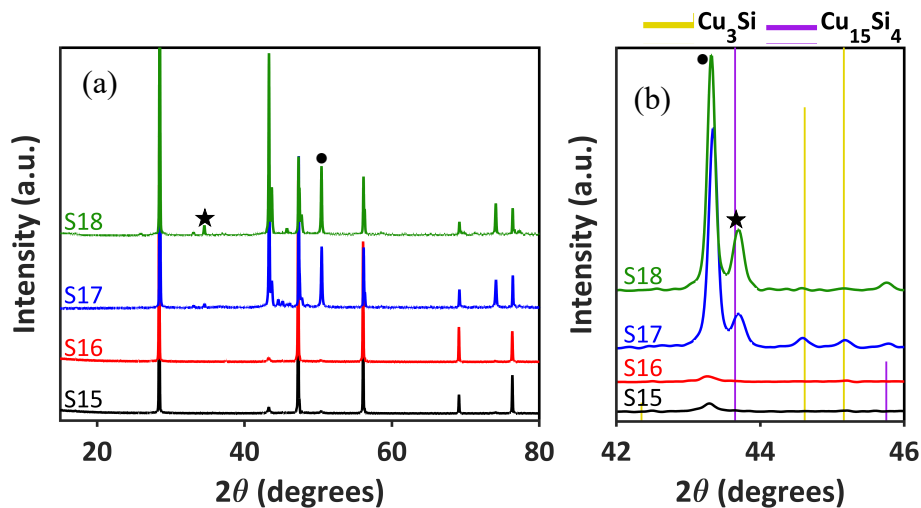


Figure 4.9: XRD spectra of S15, S16, S17 and S18 in Bragg-Brentano geometry. (a) Measured in 2θ range of 15° to 80°. ★ shows $\text{Cu}_{15}\text{Si}_4$. ● shows metallic Cu (b) Enlarged view from 2θ range of 42° to 46°. PDF (00-059-0262) for Cu_3Si , and (04-014-

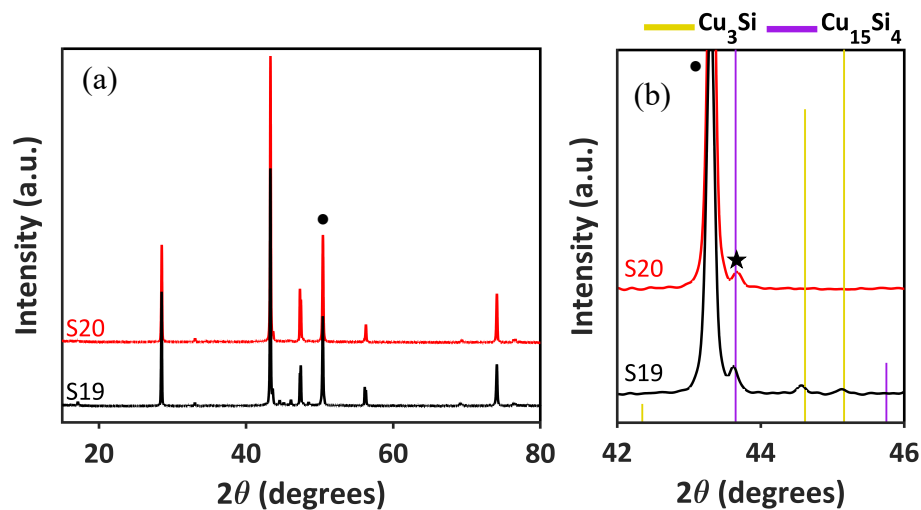


Figure 4.10: XRD spectra of S19 and S20 in Bragg-Brentano geometry (a) Measured in 2θ range of 15° to 80°. ★ shows $\text{Cu}_{15}\text{Si}_4$. ● shows metallic Cu (b) Enlarged view from 2θ range of 42° to 46°.

XRD spectrum for each contact mass sample shows the characteristic silicon peaks at 2θ values of 28.5° , 47.3° , 56.1° , 69.1° , and 76.4° . These peaks belong to the crystalline structure of silicon and have been discussed in section 4.1. XRD peaks at 2θ value of 43.3° and 50.4° belong to (1 1 1) and (2 0 0) planes of metallic copper (ICDD 00-004-0836) [80]. The characteristic XRD peaks for Cu_3Si also referred to as η -phase, are located at 2θ values of around 44.5° and 45.1° (ICDD 00-059-0262) [21], [72], [81]–[83]. The Diffractogram peaks for Cu_3Si are present in each contact mass sample, except S11 and S12, with varying intensity, as shown in Figure 4.8(b), Figure 4.9(b), and Figure 4.10(b). Another copper silicide phase, $\text{Cu}_{15}\text{Si}_4$, denoted as ϵ -phase, is also detected by the XRD at around 34.5° , 43.7° , 45.71° , 47.7° , and 58.3° 2θ values (ICDD 04-014-4307). Luo *et al.* has previously reported the presence of $\text{Cu}_{15}\text{Si}_4$ in the reacted contact mass samples [38]. Both η -phase and ϵ -phase are also plotted as their respective standard Powder Diffraction File (PDF) cards in Figure 4.8(b), Figure 4.9(b), and Figure 4.10(b).

In the XRD patterns of samples with the standard amount of CuCl – S11, S12, S15, S16 – there is no peak related to the unreacted CuCl . While for samples with five times the amount of catalyst, a small CuCl peak at 33.03° is found for S17, S18, S19, and S20, indicating the presence of unreacted CuCl . A previous study reported that the addition of CuCl in higher concentrations has an adverse effect on the selectivity, reaction rate, and induction time due to the high tendency of particle agglomeration [21]. Agglomeration of catalyst particles also leads to a higher tendency of inactive copper enrichment [21]. After 16 hours of

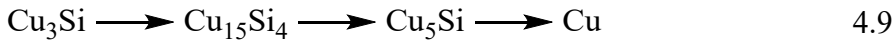
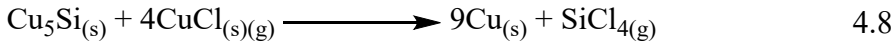
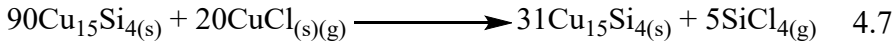
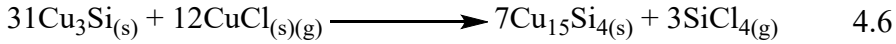
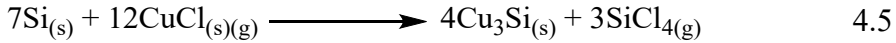
reaction, samples with five times the amount of CuCl (S17 and S18) show an intense copper peak at a 2θ value of 43.3° .

The role of Zn on Cu_xSi ($x=3, 15$) can be clearly explained by comparing the Zn-promoted samples to the samples without Zn. In Figure 4.8(b), the peaks at around 43.7° and 45.7° , attributed to $\text{Cu}_{15}\text{Si}_4$, show higher intensity for S14 (without Zn) than Zn-promoted sample S13. S18, the sample with 16 hours of reaction time in Figure 4.9, shows a much higher $\text{Cu}_{15}\text{Si}_4$ peak intensity, than the Zn-promoted S17. For samples after 40 hours of reaction time, S19 and S20, in Figure 4.10, the $\text{Cu}_{15}\text{Si}_4$ peak intensity is relatively lower and comparable. It was reported that during the course of the Rochow reaction, the quantity of ϵ -phase ($\text{Cu}_{15}\text{Si}_4$) increases initially and then tends to decrease [38].

It has been widely accepted that Zn has a positive effect on the selectivity of M2 by increasing the formation of Cu_3Si [2], [36], [42]. Five hours reacted samples S11 (Zn-promoted) and S12 (without Zn), in Figure 4.8(b), peak related to Cu_3Si alloy phase is not detected. This could be the result of the continuous consumption of the active phase [36]. For samples with 16 hours of reaction time, in Figure 4.9(b), the Cu_3Si peak intensity is more prominent for S17 (Zn-promoted) than S18 (without Zn). It should be noted that S17 is reacted with five times the amount of CuCl and Zn, while S18 only contains five times the amount of CuCl. After 40 hours of reaction time, S19 and S20 exhibit similar behavior, as shown in Figure 4.10(b).

Weber *et al.* reported that the formation of ϵ -phase ($\text{Cu}_{15}\text{Si}_4$) occurs due to the agglomeration of catalyst particles [84]. It is known that Zn acts as a dispersion agent by increasing the enrichment of silicon on the Cu-

Si alloy [30]. In the Rochow reaction, η -phase can decompose to ϵ -phase. The η -phase to ϵ -phase transformation occurs according to Equations 4.5, 4.6, 4.7, and 4.8 [84]. Equation 4.9 summarizes the process in a simplified form [85]. The presence of Zn in the contact mass increases the tendency of Cu_3Si formation and decreases the $\text{Cu}_{15}\text{Si}_4$ formation by acting as a dispersion agent [30].



It was reported that the higher concentration of $\text{Cu}_{15}\text{Si}_4$ increases the selectivity towards M2 and the reactivity in the initial phase, but the reaction stops earlier due to copper enrichment and higher coke deposition [85]. A previous study, investigating the Rochow reaction with CuO catalyst, also reported the presence of $\text{Cu}_{6.69}\text{Si}$ specie in the reacted contact mass sample [86]. However, it was not detected in any of the analyzed reacted contact mass samples.

4.3 Surface Analysis to Study Order of Coke

Raman spectroscopy has been widely utilized to investigate the degree of structural order of the carbonaceous species, and the change of order via graphitization [87]–[91]. A few problems encountered during the experimental work, related to the fluorescence effect and heterogeneous nature of contact mass, are discussed first.

4.3.6 Fluorescence in the Raman spectra

Figure 4.11 shows the Raman spectrum of sample S16 from the Raman shift value of 200 cm^{-1} to 1800 cm^{-1} . The characteristic silicon peaks at Raman shift values of 300 cm^{-1} , 420 cm^{-1} , 519 cm^{-1} , 615 cm^{-1} , and 940 cm^{-1} are discussed in section 4.1. The peaks related to the carbonaceous material are detected at around 1130 cm^{-1} , 1310 cm^{-1} , and 1600 cm^{-1} , and discussed later in section 4.3.8.

In the Raman spectrum of sample S16, the upward shift of the whole spectrum, the downward peak at around 780 cm^{-1} , and the straight line at around 1400 cm^{-1} is caused by the fluorescence phenomenon [92]. Vogelaar reported that the fluorescence effect when analyzing carbon-based material is caused by the backscattering photons of random energy [92].

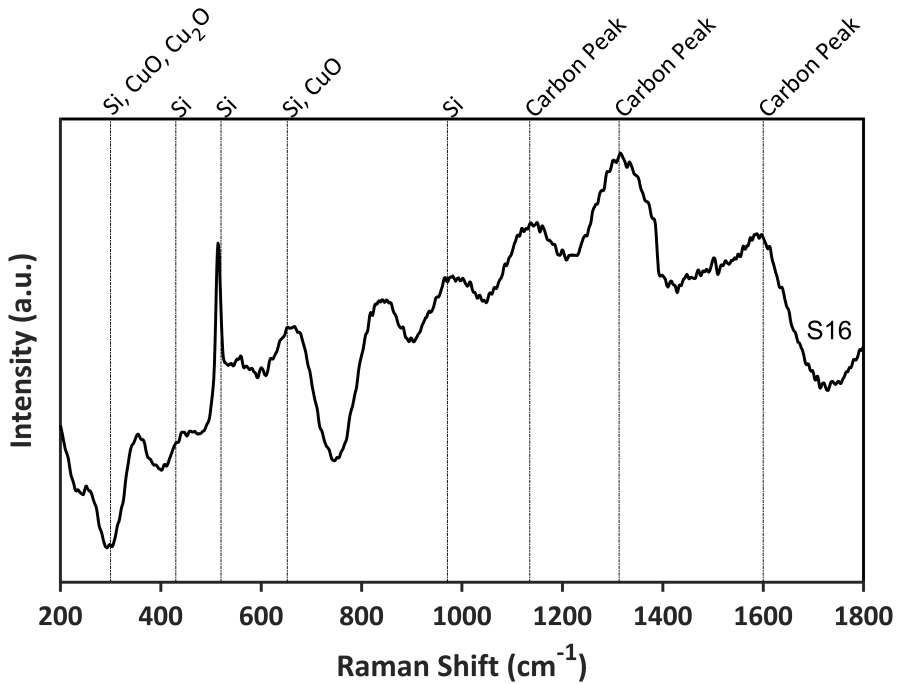


Figure 4.11: Raman spectrum of S16. Measured with 632 nm laser from Raman shift of 200 cm⁻¹ to 1800 cm⁻¹.

The ideal solution would be to switch to a laser with less power [93]. To minimize the effect of fluorescence, it has been suggested to de-focus the laser beam, optimizing the exposure time and number of accumulations [92]. These parameters were optimized for each spectrum measurement. For further analysis, each spectrum is shifted to zero intensity, and a linear baseline correction is applied using LabSpec 6 Spectroscopy software.

4.3.7 Inhomogeneous Surface Distribution

Figure 4.12 shows the Raman spectra for sample S11 (Zn-promoted with 5 hours of reaction time) at two different spots. Each spectrum is measured from the Raman shift value of 200 cm^{-1} to 1800 cm^{-1} . Both spectra have been offset along the y-axis by an arbitrary value.

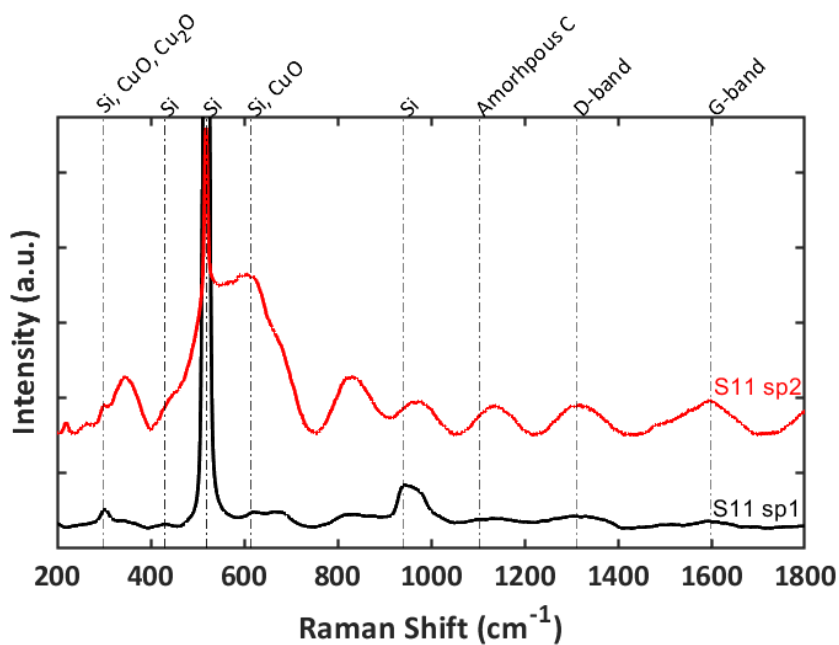


Figure 4.12: Raman spectrum of S11 at two different spots. Measured with 632 nm laser from Raman shift of 200 cm^{-1} to 1800 cm^{-1} .

The characteristic silicon peaks at Raman shift values of 300 cm^{-1} , 420 cm^{-1} , 519 cm^{-1} , 615 cm^{-1} , and 940 cm^{-1} are detected for both spots. These standard peaks belong to specific phonons of silicon and have been discussed in section 4.1. The intensity of the main silicon peak at 519 cm^{-1} for spot 2 is much lower than that of spot 1, as can be observed in Figure 4.12.

It has been known that the Raman peak intensity of a specie in a heterogeneous material is directly proportional to its relative concentration at that surface point [94], [95]. Thus, the spots that show lower intensity for the silicon could have more coke deposition on the particle surface. The carbon peaks at around 1100 cm^{-1} , 1310 cm^{-1} , and 1600 cm^{-1} for spot 2 show higher intensity than those of spot 1. Such variations in the peak intensities from spot to spot are related to the inhomogeneous distribution of surface species in the powder samples [39]. Figure A.1 shows the Raman spectra on silicon-rich spots for a few other samples. To investigate the chemistry of the coke phase with respect to reaction time, and amount of CuCl and Zn, multiple measurements are taken at different spots. An average of at least five most frequently repeating spectra is then selected for comparison and discussion.

4.3.8 Phase Chemistry of Coke

Figure 4.13 shows the Raman spectra of samples with a standard amount of CuCl, Sn, and Zn (S11 and S15) and samples with a standard amount of only CuCl and Sn (S12 and S16). It is noted that S11 and S12 are reacted for five hours, while S15 and S16 have a reaction time of 16 hours. Figure 4.14 shows the Raman spectra of samples S13, S17, S19, S14, S18, and S20 from bottom to top. S13, S17, and S19 are reacted for 5, 16, and 40 hours, respectively, with the addition of five times the amount of CuCl, Sn, and Zn. S14, S18, and S20 are also reacted for 5, 16, and 40 hours, but with five times the amount of CuCl and Sn only. Each spectrum, in both figures, is offset along the y-axis for clarity.

The peaks at Raman shift values of 300 cm^{-1} , 420 cm^{-1} , 519 cm^{-1} , 615 cm^{-1} , and 940 cm^{-1} indicate the crystalline nature of silicon and have been discussed in section 4.1 [96], [97]. The peaks at around 1120 cm^{-1} , 1310 cm^{-1} , and 1600 cm^{-1} are attributed to the carbonaceous material [87]. Tuinstra and Koenig reported that carbonaceous materials are distinguished by two main bands; the band at around 1310 cm^{-1} is called disordered (D) band, and the one at around 1600 cm^{-1} is known as the graphitic (G) band [87]. The D band at around 1310 cm^{-1} is caused by the in-plane defects of heteroatoms such as oxygen and hydrogen, and its intensity and broadness are increased in less ordered carbon [90], [98]. The G band is associated with the in-plane vibrations of aromatic carbon in the graphitic carbon structure [98]. The exact nature of the band at around 1150 cm^{-1} is not clear. Beyssac *et al.* assigned this band to poorly organized coke [99]. Guichard *et al.* assigned this peak to C-H vibrations [100]. This peak might also be related to the presence of hydrogenated coke [101].

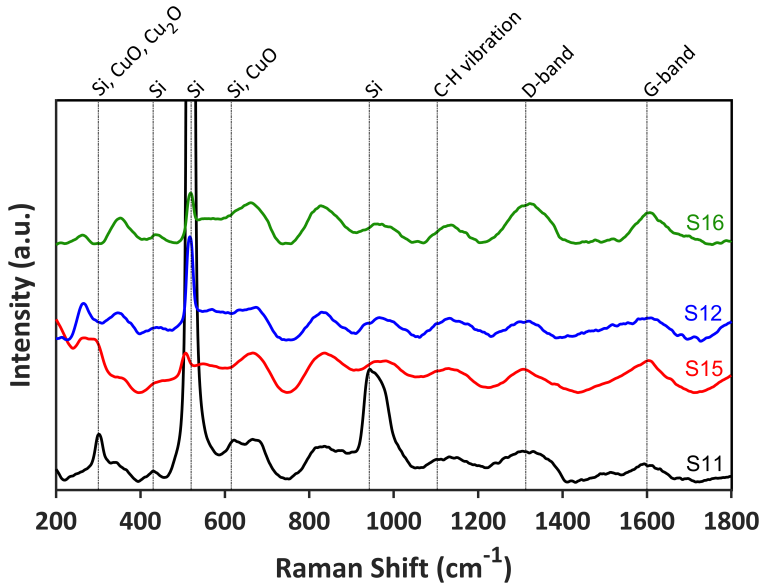


Figure 4.13: Raman spectra of S11, S15, S12 and S16 samples. Measured with 632 nm laser from Raman shift of 200 cm^{-1} to 1800 cm^{-1} .

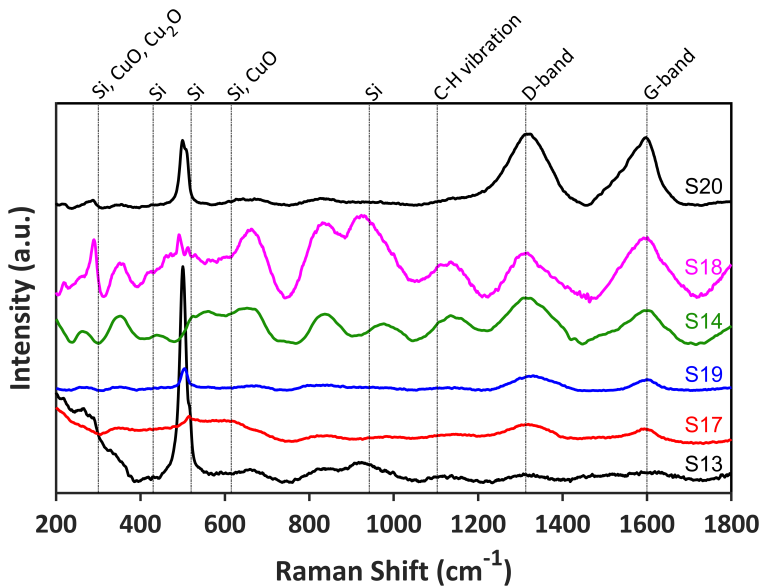


Figure 4.14: Raman spectra of S13, S17, S19, S14, S18 and S20 samples. Measured with 632 nm laser from Raman shift of 200 cm^{-1} to 1800 cm^{-1} .

S11 and S12, samples with and without Zn, respectively, show all carbonaceous peaks at around 1120 cm^{-1} , 1310 cm^{-1} , and 1600 cm^{-1} . Both samples have a reaction time of 5 hours, but S12 has a relatively less intense silicon peak. The main silicon peak at around 519 cm^{-1} is noticed to be more intense for the Zn-promoted sample S11 than that of the sample S12 (without Zn). This could be the result of the particle surface being covered by either the unreacted catalyst or the η -phase. The former point is more likely to be accurate, as the XRD diffractograms of S11 and S12, in Figure 4.8, show a very small peak intensity for Cu_3Si . Gasper-Galvin *et al.* suggested that Zn increases the dispersion of copper on the silicon surface [42]. The surface of sample S11 is more homogeneous in nature as compared to that of S12. Raman spectra of samples S13 and S14, in Figure 4.14, reveal a similar result, where the silicon peak at around 520 cm^{-1} has a higher intensity for Zn-promoted S13 than that of S14. Both samples have a reaction time of 5 hours and reacted with five times the amount of CuCl and Sn . It is noted that Sample S13 is also promoted with five times the amount of Zn. Samples with more than five hours of reaction time (S15, S16, S17, S19, and S20) do not exhibit this change in silicon peak intensity with respect to reaction time, as shown in Figure 4.13 and Figure 4.14.

A commonly used spectral feature to analyze the carbon peaks in the Raman spectrum is the ratio of D-band intensity to G-band intensity [102]. This can quantitatively provide insight into the structural order of carbon. As mentioned in section 4.3.6, Raman spectra of contact mass samples are a victim of fluorescence effect. Although an effort was made to minimize this effect by creating a baseline, the relative intensities of peaks may have changed during the process. ID/IG ratios are listed in

Table 4.1; however, ID/IG values are not used for further discussion. Another important spectral feature is the use of carbon peak width and full width at half maximum [98], [99], [103], [104]. In order to investigate the degree of structural order of the deposited carbon material, full width at half maximum (FWHM) of and G-band is discussed.

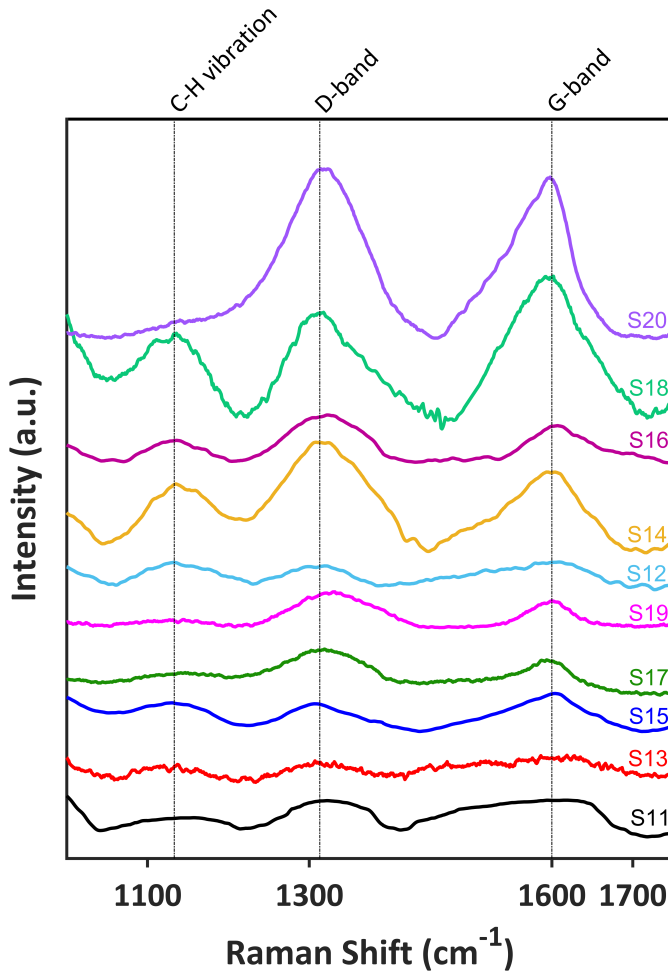


Figure 4.15: Raman spectra of reacted contact mass samples. Measured with 632 nm laser from Raman shift of 1000 cm^{-1} to 1750 cm^{-1} .

Figure 4.15 shows an enlarged view of Raman spectra of all the analyzed samples from the Raman shift value of 1000 cm^{-1} to 1750 cm^{-1} . Each spectrum is offset along the y-axis by an arbitrary value for clarity. Full width at half maximum (FWHM) values of G-band, listed in Table 4.1, are calculated using Spectragryph optical spectroscopy software [105]. S11 and S13 show that with increasing reaction time, FWHM_G value decreases from 96.68 cm^{-1} (S11) to 84 cm^{-1} (S13), as presented in Table 4.1. Similarly, S15, S17, and S19, samples with five times the amount of catalyst and Zn, show that with the increase of reaction time from 5 hours (S15) to 17 hours (S17) to 40 hours (S19), FWHM_G decreases from 113.4 cm^{-1} (S15) to 87.2 cm^{-1} to 59.2 cm^{-1} (S19), respectively. Figure 4.15 also shows that G-band changes from a broad peak to a narrower and more distinct peak, from S15 to S17 to S19, respectively. This trend of G-band indicates that graphitic carbon in the Zn-promoted contact mass samples becomes more ordered with fewer defects, as the reaction proceeds [106], [107].

On the other hand, samples reacted without the addition of Zn show the opposite behavior. FWHM_G for S12, sample reacted for 5 hours, is around 49 cm^{-1} . After 16 hours of reaction, for S16, FWHM_G increases to around 220 cm^{-1} . Samples with five times the amount of catalyst, but no Zn, demonstrate the same pattern. FWHM_G for S14 is around 113 cm^{-1} , and after 16 hours of reaction time (S18), FWHM_G increases to 121 cm^{-1} . S20, after 40 hours of reaction time, shows a higher FWHM_G of 188 cm^{-1} . This suggests that without the addition of Zn promoter, the phase of carbon changes to poorly ordered graphitic structure as the reaction proceeds [98]. Beny-bassez and Rouzaud reported that the

poorly ordered carbon in a sample with a broad G band is caused by defects in the graphitic structure [90].

Table 4.1: FWHM of and G band. ID/IG ratios for all the reacted contact mass samples.

Sample	FWHM _G (cm ⁻¹)	ID/IG ratio
S11	96.68	0.9
S12	49	0.97
S13	84	0.89
S14	112.9	1.2
S15	113.4	0.93
S16	219.88	1.03
S17	87.2	1.15
S18	121	0.93
S19	59.2	1.03
S20	188.065	1.03

Beyssac reported that the intensity of the carbon peak at around 1130 cm⁻¹ is more prominent in poorly ordered carbon [99]. Such is the case with the contact mass samples without the addition of Zn. Figure 4.15 shows a more prominent carbon peak at 1130 cm⁻¹ for samples without Zn (S12, S14, S16, S18, and S20) than for samples with Zn (S11, S13, S15, S17, and S19). Contact mass samples reacted without the addition

of Zn exhibit higher D-band intensity than Zn-promoted samples, as shown in Figure 4.15. This relatively intense D-band, in samples without Zn, attests to the highly disordered carbon, due to the presence of aromatic species [108]. The investigation of carbon peaks demonstrates that the presence of Zn as a promoter tends to change the phase of the deposited carbon to a more structurally ordered carbon.

4.4 Effect of Zn on the Reactivity of Coke

Surface analysis of deposited coke by Raman shed light on how the structural order of coke is affected by the Zn promoter and its evolution over reaction time. Thermogravimetric analysis (TGA) coupled with mass spectrometry (MS), in the oxidative atmosphere, is utilized to study the effect of Zn on the reactivity of coke in the bulk of the contact mass. The results of TGA/MS analysis carried out in an inert atmosphere for all the samples are given in Figure A.8 to Figure A.15. It is noted that S13 and S14 are not analyzed with TGA. For the sake of convenience, this section is divided into two sub-sections: samples with Zn, and samples without Zn. The results are then compared and discussed.

4.4.9 Samples with Zn

Figure 4.16 and Figure 4.17 show the thermogravimetric analysis (TGA), differential scanning calorimetry (DSC) and mass spectrometry (MS) results for sample S11 and S15, respectively, in the oxidative atmosphere. Both S11 and S15 samples are promoted with Zn and Sn, where S11 has a reaction time of 5 hours, and S15 is reacted for 16 hours. Sample S11, in Figure 4.16(a), shows slight variations in the TGA curve, while sample S15, in Figure 4.17(a), experiences a continuous mass loss over the whole temperature range, with an overall mass loss of around 2.5 %. Below 100 °C, the mass loss in sample S11 is negligible. However, for S15, the mass loss below 100 °C is observed to be more than 1 %. This mass change is attributed to the drying process of water and dehydration of Si-OH groups present in the reacted contact mass sample [109]. The corresponding MS ion current curves for water

($m/z=18$) in Figure 4.17(b) for S15 provides a validation that this initial mass loss is indeed due to the removal of H_2O .

The MS ion current curve for CO_2 ($m/z=44$), in Figure 4.16(b) and Figure 4.17(b), shows the formation of carbon dioxide. The CO_2 MS spectrum for S11 starts at a temperature of $180\text{ }^\circ\text{C}$, with a peak at $336\text{ }^\circ\text{C}$, and there is no indication of accompanying water MS spectrum ($m/z=18$) at this temperature. For S15, the CO_2 MS spectrum starts to show at a relatively higher temperature of $200\text{ }^\circ\text{C}$, with a peak at $300\text{ }^\circ\text{C}$. Similar to S11, the CO_2 MS spectrum is not accompanied by an H_2O MS signal ($m/z=18$) at this temperature. The TGA and DSC curves of S11 and S15 do not indicate any distinct change at the formation temperature of CO_2 . This could be the result of either simultaneous oxidation of silicon and copper species in the sample or due to a small quantity of carbonaceous material being decomposed.

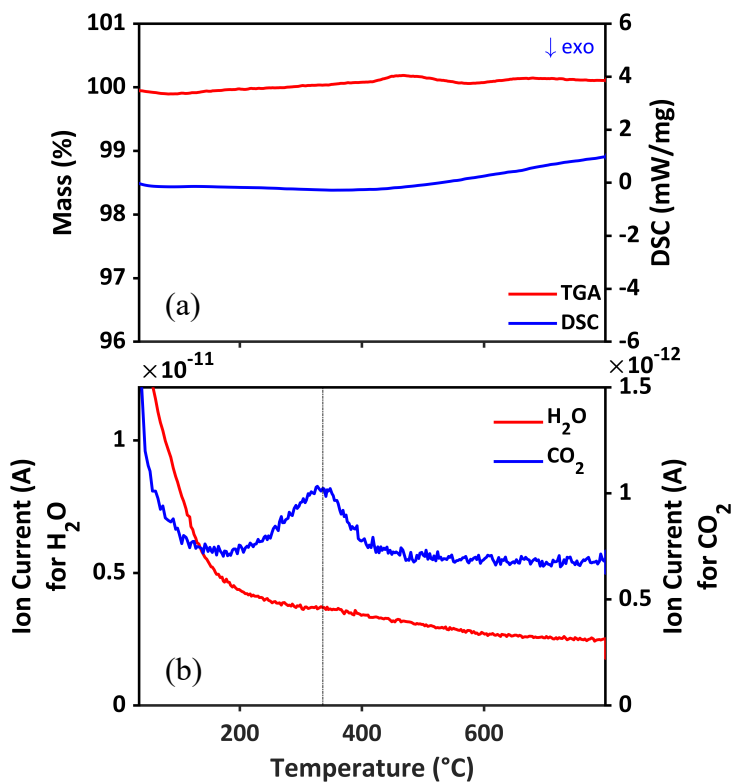


Figure 4.16: TGA, DSC and MS analysis of S11 in oxidative atmosphere (55 ml/min air and 25 ml/min argon) from 35 °C to 800 °C at 10 °C/min heating rate. **(a)** TGA curve on the left and DSC curve on the right **(b)** MS ion current for H₂O ($m/z=18$) on the left and CO₂ ($m/z=44$) on the right.

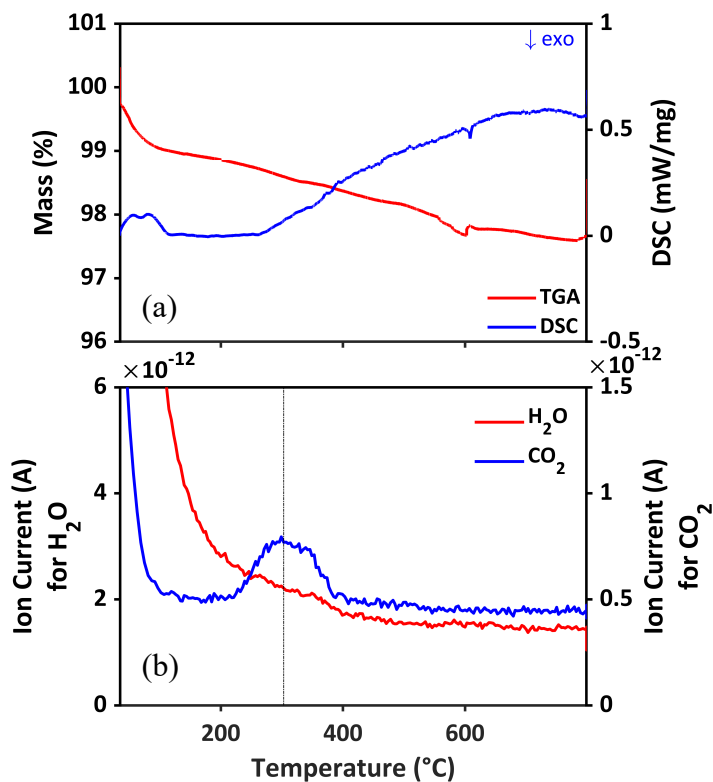


Figure 4.17: TGA, DSC and MS analysis of S15 in oxidative atmosphere (55 ml/min air and 25 ml/min argon) from 35 °C to 800 °C at 10 °C/min heating rate. (a) TGA curve on the left and DSC curve on the right (b) MS ion current for H₂O ($m/z=18$) on the left and CO₂ ($m/z=44$) on the right.

Figure 4.18 and Figure 4.19 show the TGA, DSC, and MS results for S17 and S19; these samples are promoted with five times the amount of CuCl, Sn, and Zn. S17 and S19 have a reaction time of 16 and 40 hours, respectively. The thermal analysis is carried out in an oxidative atmosphere from 35 °C to 800 °C at a heating rate of 10 K/min.

Below 100 °C, samples S17 and S19 experience a mass loss of around 1.5 % and 4 %, respectively, as demonstrated by the respective TGA curves in Figure 4.18(a) and Figure 4.19(a). The H₂O MS spectrum ($m/z=18$) of S17 and S19 are presented in Figure 4.18(b) and Figure 4.19(b), which show the drying process below 100 °C in the form of a decreasing slope around 100 °C.

From 100 °C to around 420 °C, S17 sees a slight mass increase, while S19 undergoes an initial mass decrease and then increase. This can be attributed to the combined effect of mass loss by decomposition of carbonaceous species and mass increase by the oxidation of silicon and copper species. The disadvantage of TGA is again underlined here, as it is not possible to distinguish between these two phenomena just by analyzing the TGA curve. Wessel reported that during the oxidative TGA analysis, the oxidation of silicon and copper species occurs and makes it impossible to draw a baseline [41]. The exothermic DSC peak, at 294 °C for S17 and at 264°C for S19, corresponds to the formation of CO₂ by decomposition of carbon material.

In S17 and S19, the substantial mass decrease from 420 °C to 800 °C is caused by the decomposition of unreacted CuCl in the contact mass. A detailed discussion of the thermal analysis of CuCl is presented in section 4.1.

The CO₂ MS signal for S17, in Figure 4.18(b), shows the starting temperature and peak temperature is 167 °C and 294 °C, respectively. In Figure 4.19(b), sample S19 shows a narrow CO₂ MS signal with a starting temperature of 198 °C and a peak temperature of 264 °C. An exothermic peak in the DSC curves of sample S17 and S19 occurs at 294 °C and 264 °C, respectively. This peak is the combined effect of the decomposition of carbonaceous species and the successive formation of CO₂.

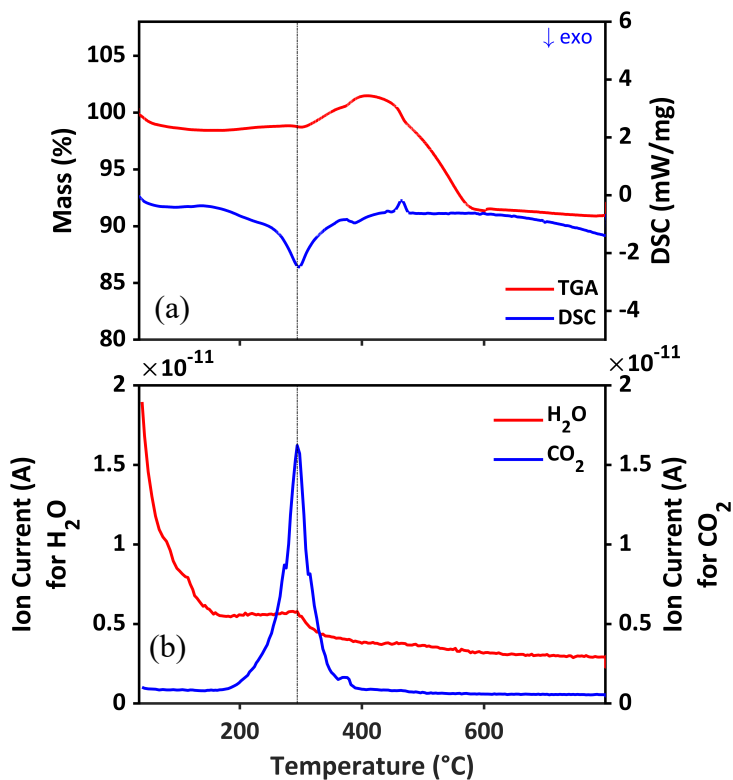


Figure 4.18: TGA, DSC and MS analysis of S17 in oxidative atmosphere (55 ml/min air and 25 ml/min argon) from 35 °C to 800 °C at 10 °C/min heating rate. (a) TGA curve on the left and DSC curve on the right (b) MS ion current for H₂O ($m/z=18$) on the left and CO₂ ($m/z=44$) on the right.

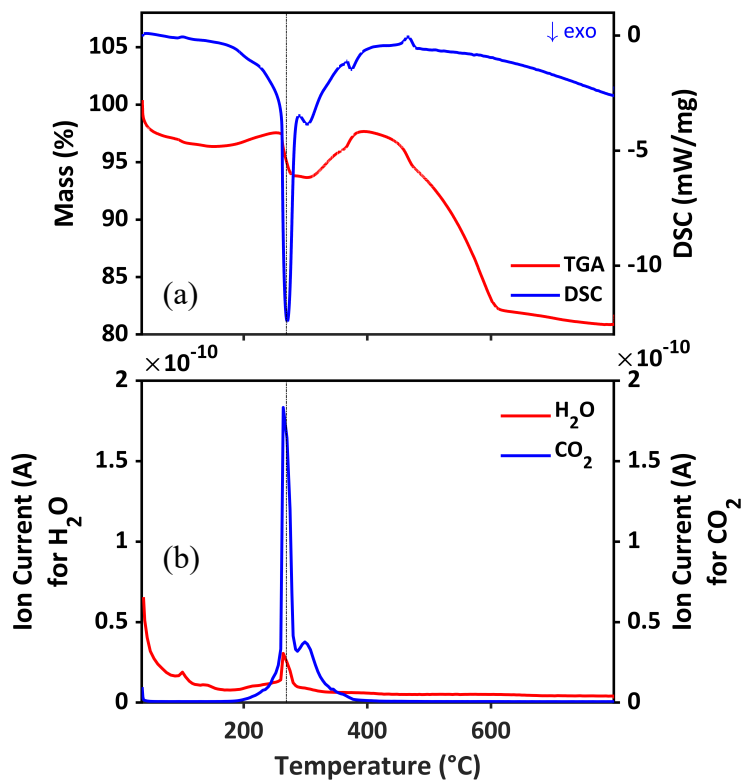


Figure 4.19: TGA, DSC and MS analysis of S19 in oxidative atmosphere (55 ml/min air and 25 ml/min argon) from 35 °C to 800 °C at 10 °C/min heating rate. **(a)** TGA curve on the left and DSC curve on the right **(b)** MS ion current for H₂O ($m/z=18$) on the left and CO₂ ($m/z=44$) on the right.

4.4.10 Samples without Zn

The TGA, DSC, and MS analyses of samples S12 and S16, both without Zn and a reaction time of 5 hours and 16 hours, respectively, are presented in Figure 4.20 and Figure 4.21. Figure 4.22 and Figure 4.23 show the TGA/MS results for samples S18, and S20, both with five times the amount of CuCl and Sn, and a reaction of 16 hours and 40 hours, respectively. It is stated that S18 and S20 are not promoted with Zn.

The TGA curve for sample S12 shows an overall mass change of less than 1 %. The TGA curve for sample S16 experiences a mass loss of around 2 % below 100 °C due to the removal of water, as demonstrated by the H₂O ($m/z=18$) MS signal in Figure 4.21(b). It is observed that S16 undergoes an overall mass loss of 3 %. The CO₂ MS spectrum for both samples, in Figure 4.20(b) and Figure 4.21(b), shows a broad peak with a double shoulder, first at around 300 °C and then at around 340 °C. The CO₂ MS signal for S12 and S16 has an initial temperature of 158 °C and 168 °C, respectively.

Figure 4.22(a) and Figure 4.23(a) show that the samples with five times the amount of CuCl and Sn, S18 and S20, undergo a mass loss of around 1 to 2 % below 100 °C due to drying, as evidenced by the relative H₂O MS spectra in Figure 4.22(b) and Figure 4.23(b), respectively. As discussed earlier, the mass loss below 100 °C in all the reacted contact mass samples could be the combined results of the removal of water and dehydration of Si-OH bonds [109], [110].

From 100 °C to 400 °C, S16 and S12 go through a mass increase due to oxidation of copper and silicon species. XRD spectra of S18 in Figure

4.9 and S19 in Figure 4.10 reveal a high concentration of metallic copper in these samples. Clarke reported that free copper is very prone to oxidation [27]. Such is the case with S17 and S19 as well; the mass decreases after 420 °C in S18, and S20 is the result of the decomposition of unreacted CuCl.

The CO₂ MS signals for S18 and S20 show a distinct and narrow peak at around 300 °C. The starting temperature of CO₂ formation for both samples is around 200 °C. The DSC signal for S18 and S20 shows an exothermic peak at around 300 °C, which is related to the decomposition of carbonaceous species and the formation of CO₂. From 100 °C to 400 °C, a mass increase is observed in sample S18 and S20. XRD analysis of S18 and S20, in Figure 4.9 and Figure 4.10, respectively, shows an intense Cu peak for both samples.

From 420 °C to 800 °C, S18 and S20 go through a substantial mass loss of 8 % and 18 %, respectively. As discussed in section 4.1, the decomposition temperature of CuCl is 420 °C. This mass loss in S18 and S20, samples with five times the amount of CuCl and Sn, is related to the decomposition of the unreacted CuCl.

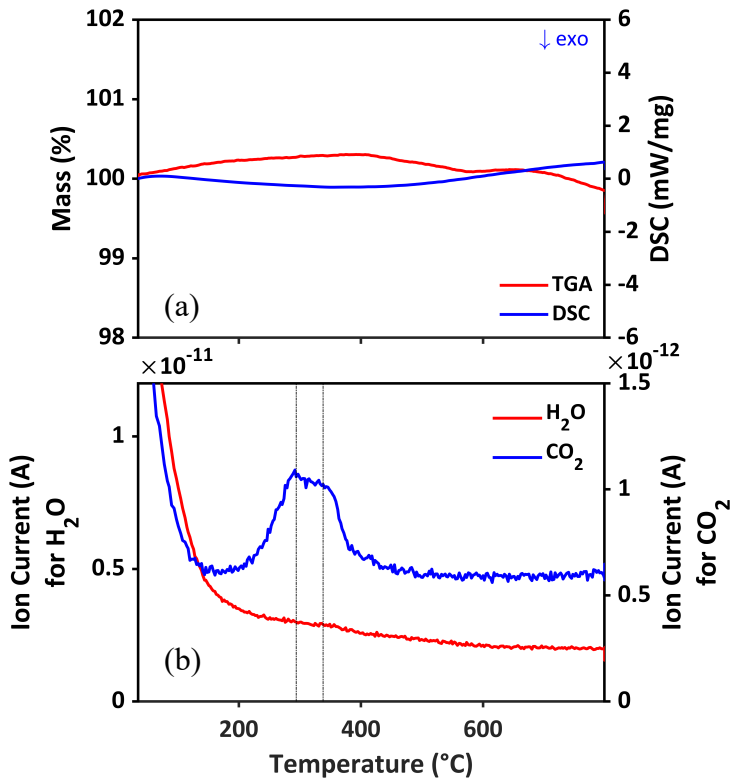


Figure 4.20: TGA, DSC and MS analysis of S12 in oxidative atmosphere (55 ml/min air and 25 ml/min argon) from 35 °C to 800 °C at 10 °C/min heating rate. (a) TGA curve on the left and DSC curve on the right (b) MS ion current for H₂O ($m/z=18$) on the left and CO₂ ($m/z=44$) on the right.

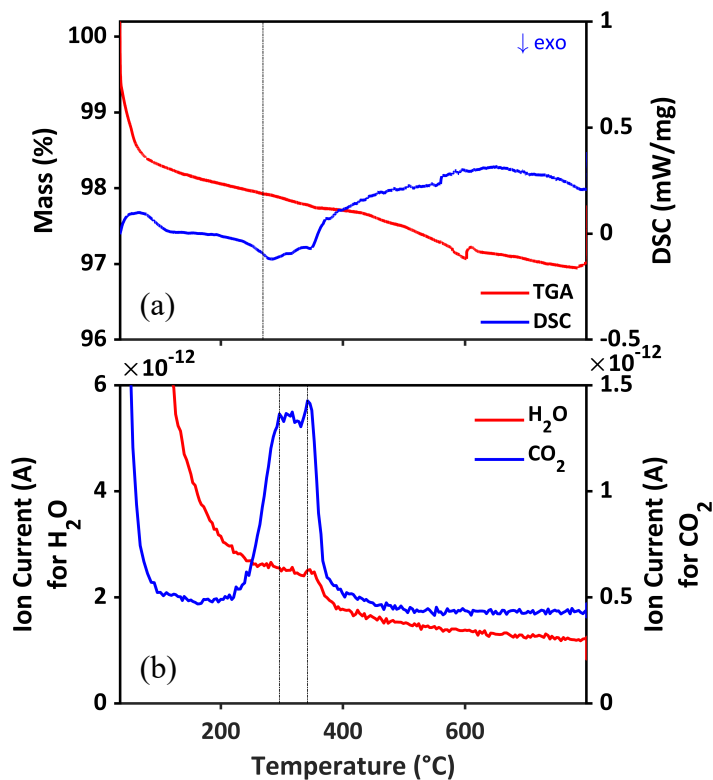


Figure 4.21: TGA, DSC and MS analysis of S16 in oxidative atmosphere (55 ml/min air and 25 ml/min argon) from 35 °C to 800 °C at 10 °C/min heating rate. (a) TGA curve on the left and DSC curve on the right (b) MS ion current for H₂O ($m/z=18$) on the left and CO₂ ($m/z=44$) on the right.

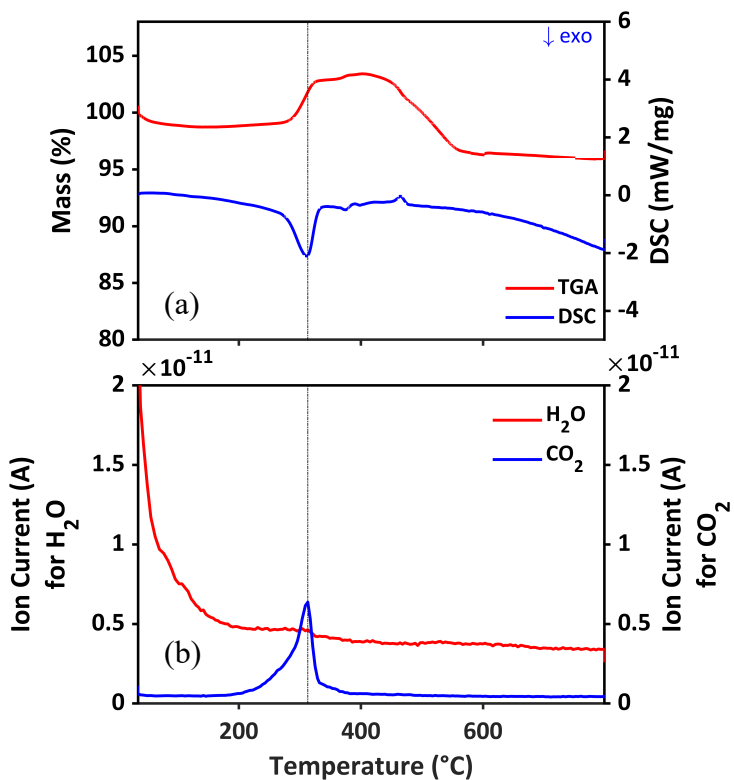


Figure 4.22: TGA, DSC and MS analysis of S18 in oxidative atmosphere (55 ml/min air and 25 ml/min argon) from 35 °C to 800 °C at 10 °C/min heating rate. (a) TGA curve on the left and DSC curve on the right (b) MS ion current for H₂O ($m/z=18$) on the left and CO₂ ($m/z=44$) on the right.

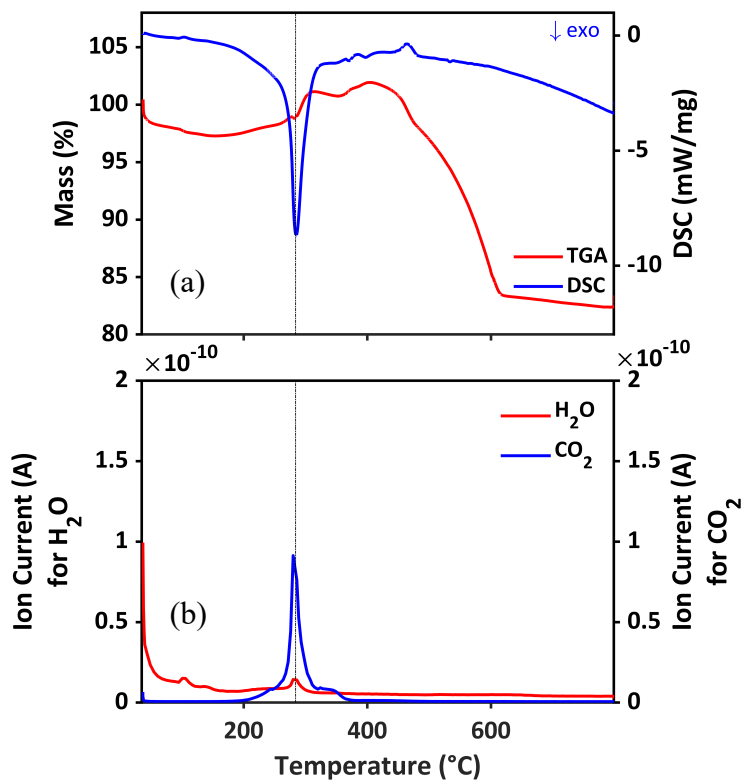


Figure 4.23: TGA, DSC and MS analysis of S20 in oxidative atmosphere (55 ml/min air and 25 ml/min argon) from 35 °C to 800 °C at 10 °C/min heating rate. **(a)** TGA curve on the left and DSC curve on the right **(b)** MS ion current for H₂O ($m/z=18$) on the left and CO₂ ($m/z=44$) on the right.

4.4.11 Comparison of Coke Reactivity

A summary of initial temperatures and peak temperatures of CO₂ formation, along with the calculated H/C ratios for all the analyzed samples is listed in Table 4.2. H/C ratios are calculated using Equation 4.10. A_{H₂O} and A_{CO₂} in Equation 4.10 correspond to the area under the curve of H₂O MS peak, and CO₂ MS peak of a reacted contact mass sample, respectively. A_{H₂O} and A_{CO₂} in Equation 4.11 correspond to the area under the curve of H₂O MS peak and CO₂ MS peak of NaHCO₃ sample, respectively.

$$H / C = \frac{A_{H_2O}}{A_{CO_2}} \times RF \quad 4.10$$

$$RF = \frac{2A_{CO_2}}{A_{H_2O}} \quad 4.11$$

Figure A.16 shows the mass spectrometry results of NaHCO₃ in the oxidative atmosphere. The correlation factor, RF, is calculated from the oxidative TGA/MS of NaHCO₃ since the H/C for NaHCO₃ is one. It was noticed that the calculated H/C values could be unreliable due to the non-quantitative nature of the available mass spectrometry instrument. Further discussion on the reactivity of coke is, thus, based on the oxidation temperatures of coke.

In all the contact mass samples, the initial temperature of oxidation of coke is below 300 °C, as shown in Table 4.2. It was reported that the coke oxidized below 400 °C is to be attributed to soft coke, and it

consists of amorphous structures, alkylated mono-aromatics, and di-aromatics [111]. On the other hand, hard coke has a higher oxidization temperature and comprises of poly-condensed aromatics [111]. Another study reported that hard coke is oxidized above 600 °C [73]. Thermal analysis of the reacted contact mass samples does not show any presence of hard coke. The presence of hard coke implies a high degree of graphitization of coke and shows a Raman peak at Raman shift value of around 2700 cm^{-1} [99], [101], [112]. However, as seen in Figure 4.15, reacted contact mass samples show the carbon material peaks below 2000 cm^{-1} only.

Table 4.2: Temperature profile of CO₂ formation and H/C ratios of all the reacted contact mass samples.

Sample	Initial temp of CO ₂ MS	The peak temperature of CO ₂ MS	End temp of CO ₂ MS	Shoulder peak temp	H/C ratio
-	(°C)	(°C)	(°C)	(°C)	-
S11	< 200	336	440	-	<0.01
S15	< 200	300	440	-	<0.01
S17	< 200	~300	410	-	0.28
S19	< 200	~260	400	-	0.37
S12	< 200	300	480	340	<0.01
S16	< 200	300	470	340	0.37
S18	< 200	~300	380	340	0.06
S20	< 200	~290	380	340	0.32

The deposited coke in every contact mass sample is soft coke in nature but with varying reactivity, as can be noticed from the peak temperature of CO₂ formation.

Zn-promoted samples, S11 and S15, show that reactivity of coke is increasing with reaction time. Peak coke oxidation temperature of five hours reacted sample, S11, is around 340 °C. After 16 hours of reaction time, the peak coke oxidation temperature has decreased to 300 °C in S15. This effect is amplified in samples with five times the amount of Zn: S17 with 16 hours of reaction time, and S19 with 40 hours of reaction time. MS CO₂ peak of S19 is very narrow as compared to that of S17. After 40 hours of reaction time, S19 has a high reactive coke, with a peak temperature of around 260 °C. A peculiar behavior was noticed during the Raman analysis of S19. Oxidation of surface coke started to occur during the Raman spectroscopy if the laser was focused for more than 5 minutes. This was observed only in sample S19. Figure 4.24 shows the Raman spectrum of a specific spot of S19 before and after 5 minutes of exposure to the laser [113]. Figure A.2 shows the microscopic image of this S19 spot before and after laser exposure. Vogelaar noticed a similar incident and reported that this effect shows the high reactivity of coke [92].

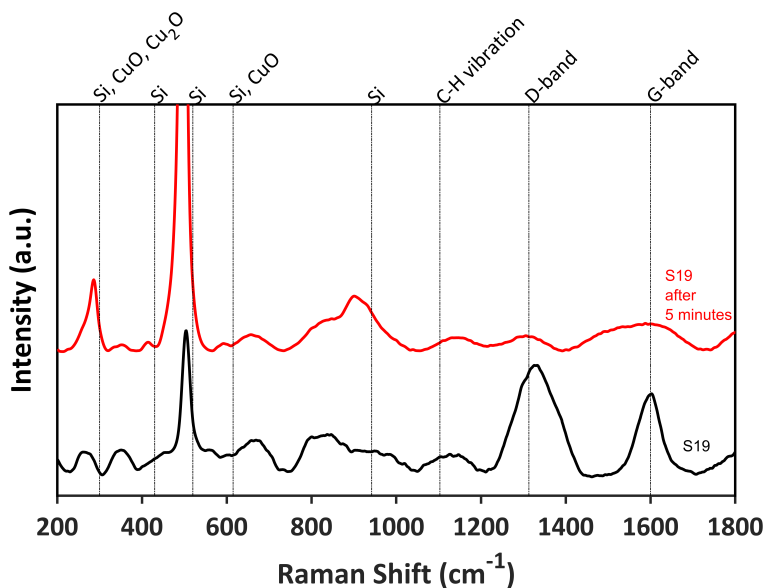


Figure 4.24: Raman spectra of S19 at the same spot. Measured with 632 nm laser from Raman shift of 200 cm^{-1} to 1800 cm^{-1} .

For Samples reacted with the addition of a standard amount of CuCl and Sn but no Zn, named S12 (5 hours reaction time) and S16 (16 hours of reaction), the peak temperature of the CO_2 formation remains the same with respect to the reaction time. Both samples show a second peak at around 340 °C, indicating that coke in these samples is less reactive than S11 and S15. S18 (16 hours reaction time) and S20 (40 hours reaction time), samples without Zn but five times the amount of CuCl and Sn, however, do not follow this trend. After 40 hours of reaction time, S20 shows a peak temperature of 290 °C.

During the thermal analysis, the sample mass was kept the same for each measurement. A comparison of the mass spectrum of S11 and S12 shows that the CO_2 signal of S12 has a higher peak intensity than the Zn-promoted S11. S12 also shows a broader CO_2 peak with a shoulder peak.

Similar behavior is noticed when comparing the MS CO₂ spectrum of Zn-promoted S15 to S16. CO₂ peak intensity of S16 is much higher with a shoulder peak. The results are in agreement with a previous study reported by Wessel [41]. It was reported that contact mass samples reacted without Zn had a higher deposition of coke. Wessel categorized the coke into two types: α -coke, which is oxidized at a lower temperature, and β -coke, which is oxidized at higher temperatures [41]. It was suggested that only β -coke is responsible for the catalyst deactivation as it is deposited on the active surface sites [41]. The first shoulder of CO₂ MS signal in S12 and S16 can be assigned to α -coke and the second shoulder to the β -coke. Zn-promoted samples, S11, S12, S17, and S19, reveal only a single CO₂ MS peak. As discussed in section 4.2, Zn-promoted samples have a high tendency of active site formation. The CO₂ in Zn-promoted samples could belong to the β -coke. This investigation is in agreement with the previous study on catalyst deactivation by coke formation in the Rochow reaction [41].

5 Conclusion

The thesis work on the direct synthesis of dimethyldichlorosilane was performed with the aim of investigating the role of catalyst precursor CuCl, reaction time, and zinc (Zn) promoter on the formation of the η -phase Cu₃Si, its transformation to Cu₁₅Si₄, and the deactivation process. The research on the catalyst deactivation by coke formation is of particular importance, as there are few reported studies on it, in spite of its impact on the industrial-scale operation. To be able to distinguish the type of coke deposited on the active sites, it was deemed essential to study the properties of the formed coke, such as the degree of structural order of coke and changes in the reactivity with respect to reaction time, and concentration of CuCl and Zn. For this purpose, the CuCl sample, unreacted contact mass sample (S0), and a series of reacted contact mass samples with varying reaction time, and concentrations of CuCl and Zn were analyzed with x-ray diffraction (XRD), Raman spectroscopy, and thermogravimetric analysis coupled with mass spectroscopy (MS).

It was found that the concentration of CuCl and Zn has a controlling effect on the formation of Cu₃Si and its transformation to Cu₁₅Si₄ during the reaction. XRD analysis shows that, in samples promoted with the standard amount of CuCl and Zn (S11 and S15), the tendency of Cu₃Si to Cu₁₅Si₄ transformation is less, and there is very low enrichment of inactive copper, due to the promoting ability of Zn to act as a dispersion agent. Samples with five times the amount of CuCl and Zn (S13, S17, and S19) reveal a higher tendency of Cu₃Si to Cu₁₅Si₄ conversion during the reaction. For samples without the addition of Zn (S12, S14, S16, S18, and S20), the agglomeration of catalyst particles leads to high

enrichment of inactive copper and enhanced presence of $\text{Cu}_{15}\text{Si}_4$. This is consistent with the previously reported studies on the role of Zn as a dispersion agent. A previous study reported that the formation of $\text{Cu}_{15}\text{Si}_4$ results in reaction activity loss due to an extra step of decomposition of $\text{Cu}_{15}\text{Si}_4$ to Cu_3Si , as discussed in section 4.2. The enrichment of free copper in samples without Zn may also be the result of high coke formation, as the coke formed on the active catalytic sites leads to the deactivation of free active copper (Cu^*).

The use of Raman spectroscopy and thermogravimetric analysis to study the structural order and reactivity of coke, respectively, proved to be challenging but valuable. It was observed that in Zn-promoted samples (S11, S13, S15, S17, and S19), as the reaction time increases, the structure of carbon becomes more ordered with fewer defects, while in samples reacted without the addition of Zn (S12, S14, S16, S18, and S20), phase of carbon changes to a structure of less order with an increase in reaction time. The increasing disorder of the coke in samples without Zn with respect to reaction time is the result of aromatic species. Thermal analysis showed that coke formed in all the reacted contact mass samples is soft coke, which starts to oxidize at around 200 °C. The Zn-promoted samples show that the reactivity of coke increases with reaction time, and the MS ($m/z=44$) CO_2 peak becomes more distinct and narrower. The CO_2 MS signal in samples reacted without the addition of Zn (S12, S14, S16, S18, and S20) is broad with a shoulder peak at around 340 °C, leading to a conclusion that these samples contain relatively less reactive coke.

6 Future Work

Several aspects of Cu_3Si formation and coke deposition on the active sites need to be further investigated. X-ray analysis clearly indicated the tendency of Cu_3Si formation with respect to reaction time and the presence of Zn. However, a more quantitative approach is needed to conclude the discussion on the role of Zn. Zhang employed aqueous selective leaching of Cu_3Si from the reacted contact mass [114]. It was reported that the Cu_3Si alloy phase could be separated by dissolving the reacted contact mass in a mixture of NH_4OH and H_2O , and then further analyzed [114].

As discussed in section 4.3, Raman spectroscopy is a commonly used technique to characterize the structural order of carbon and, a crucial spectral feature of this technique is the ratio of intensities of D-band and G-band (ID/IG). However, the use of the ID/IG ratio is of less value if the spectrum is affected by the fluorescence phenomenon, as the fluorescence phenomenon affects the relative intensities of D-band and G-band peaks (section 4.3.6). The use of a laser with a lower wavelength is recommended for carbon-containing samples [115]. Quantification of coke by using temperature-programmed oxidation technique, as detailed by Wessel and Rethwisch, would further clarify how the quantity of formed coke varies as the reaction proceeds [41].

Surface analysis of reacted contact mass samples with scanning electron microscopy (SEM) to study the localized coke hotspots could not be carried out due to restricted laboratory access caused by the COVID-19 pandemic. The buildup of coke on the surface and enrichment of inactive

copper is to be studied by using scanning electron microscopy (SEM) coupled with energy-dispersive spectroscopy (EDS).

Bibliography

- [1] D. Seyferth, “Dimethyldichlorosilane and the Direct Synthesis of Methylchlorosilanes. The Key to the Silicones Industry † ,” *Organometallics*, vol. 20, no. 24, pp. 4978–4992, Nov. 2001, doi: 10.1021/om0109051.
- [2] W. J. Ward, A. Ritzer, K. M. Carroll, and J. W. Flock, “Catalysis of the Rochow Direct Process,” *J. Catal.*, vol. 100, no. 1, pp. 240–249, Jul. 1986, doi: 10.1016/0021-9517(86)90089-8.
- [3] C. Corden, D. Tyrer, H. Menadue, J. Calero, J. Dade, and R. Leferink, “The Socioeconomic Impact of the Silicones Industry in Europe,” 2015.
- [4] Z. Zhang *et al.*, “Facile synthesis of mesoporous Cu₂O microspheres with improved catalytic property for dimethyldichlorosilane synthesis,” *Ind. Eng. Chem. Res.*, vol. 51, no. 3, pp. 1264–1274, Jan. 2012, doi: 10.1021/ie2020747.
- [5] J. Li *et al.*, “ZnO supported on Cu₂O{1 0 0} enhances charge transfer in dimethyldichlorosilane synthesis,” *J. Catal.*, vol. 374, pp. 284–296, Jun. 2019, doi: 10.1016/j.jcat.2019.02.029.
- [6] A. R. L. Colas, “Silicones : Preparation , Properties and Performance.” 2005.
- [7] R. R. LeVier, M. C. Harrison, R. R. Cook, and T. H. Lane, “What is silicone?,” *J. Clin. Epidemiol.*, vol. 48, no. 4, pp. 513–517, Apr. 1995, doi: 10.1016/0895-4356(94)00207-7.
- [8] E. Yilgör and I. Yilgör, “Silicone containing copolymers:

- Synthesis, properties and applications,” *Prog. Polym. Sci.*, vol. 39, no. 6, pp. 1165–1195, Jun. 2014, doi: 10.1016/j.progpolymsci.2013.11.003.
- [9] W. Kalchauer and B. Pachaly, “Muller-Rochow Synthesis: The Direct Process to Methylchlorosilanes,” in *Handbook of Heterogeneous Catalysis*, Weinheim, Germany: Wiley-VCH Verlag GmbH & Co. KGaA, 2008, pp. 2635–2647.
- [10] Y. Zhang, J. Li, H. Liu, Y. Ji, Z. Zhong, and F. Su, “Recent Advances in Rochow-Müller Process Research: Driving to Molecular Catalysis and to A More Sustainable Silicone Industry,” *ChemCatChem*, vol. 11, no. 12, pp. 2757–2779, Jun. 2019, doi: 10.1002/cctc.201900385.
- [11] L. Lewis, W. Ligon, and J. Carnahan, “A study of copper oxide catalysts used in the methylchlorosilane reaction and determination of the fate of oxygen,” *Silicon Chem.*, vol. 1, no. 1, pp. 23–33, 2002, doi: 10.1023/A:1016042519686.
- [12] X. Chen *et al.*, “Solvothermal synthesis of copper (I) chloride microcrystals with different morphologies as copper-based catalysts for dimethyldichlorosilane synthesis,” *J. Colloid Interface Sci.*, vol. 404, pp. 16–23, Aug. 2013, doi: 10.1016/j.jcis.2013.04.028.
- [13] J. Stein, “Catalyzed Direct Reactions of Silicon,” *Appl. Catal. A Gen.*, vol. 112, no. 1, pp. N15–N16, May 1994, doi: 10.1016/0926-860x(94)80152-5.
- [14] J. Acker, S. Köther, K. M. Lewis, and K. Bohmhammel, “The reactivity in the system CuCl-Si related to the activation of silicon

- in the Direct Synthesis,” *Silicon Chem.*, vol. 2, no. 3/4, pp. 195–206, May 2003, doi: 10.1023/B:SILC.0000046751.05300.d4.
- [15] P. P. Singhania, G. K. Wattal, and D. Kunzru, “Modelling of the reaction between methyl chloride and silicon,” *Chem. Eng. Sci.*, vol. 38, no. 3, pp. 469–471, 1983, doi: 10.1016/0009-2509(83)80163-8.
- [16] K. Kumbilieva, L. Petrov, Y. Alhamed, and A. Alzahrani, “Reaction mechanism and deactivation modes of heterogeneous catalytic systems,” *Cuihua Xuebao/Chinese Journal of Catalysis*, vol. 32, no. 3. Elsevier, pp. 387–404, Mar. 01, 2011, doi: 10.1016/s1872-2067(10)60181-7.
- [17] P. G. Menon, “Coke on catalysts-harmful, harmless, invisible and beneficial types,” *J. Mol. Catal.*, vol. 59, no. 2, pp. 207–220, 1990, doi: 10.1016/0304-5102(90)85053-K.
- [18] D. T. Hurd and E. G. Rochow, “On the Mechanism of the Reaction between Methyl Chloride and Silicon-Copper,” *J. Am. Chem. Soc.*, vol. 67, no. 7, pp. 1057–1059, Jul. 1945, doi: 10.1021/ja01223a007.
- [19] R. J. H. Voorhoeve and J. C. Vlugter, “Mechanism and kinetics of the metal-catalyzed synthesis of methylchlorosilanes. IV. The mechanism of the synthesis of dimethyldichlorosilane from silicon and methyl chloride,” *J. Catal.*, vol. 4, no. 2, pp. 220–228, Apr. 1965, doi: 10.1016/0021-9517(65)90012-6.
- [20] V. Bažant, “Direct Synthesis of organohalogenosilanes,” *Pure Appl. Chem.*, vol. 13, no. 1–2, pp. 313–328, Jan. 1966, doi: 10.1351/pac196613010313.

- [21] L. Zhang, J. Li, K. Yang, C. Hu, S. Ge, and C. Yang, "Effects of CuCl source and content on direct synthesis of triethoxysilane from silicon and ethanol," *Adv. Mater. Res.*, vol. 233–235, pp. 1534–1539, 2011, doi: 10.4028/www.scientific.net/AMR.233-235.1534.
- [22] D.-H. Sun, A. B. Gurevich, L. J. Kaufmann, B. E. Bent, A. P. Wright, and B. M. Naasz, "A new approach to understanding the Rochow process: synthesis of methylchlorosilanes from CH₃+Cl monolayers on Cu₃Si in vacuum," in *Studies in Surface Science and Catalysis*, vol. 101 A, Elsevier, 1996, pp. 307–315.
- [23] T. C. Frank and J. L. Falconer, "Surface compositions of copper-silicon alloys," *Appl. Surf. Sci.*, vol. 14, no. 3–4, pp. 359–374, Mar. 1983, doi: 10.1016/0378-5963(83)90049-1.
- [24] K. M. Lewis, D. McLeod, B. Kanner, J. L. Falconer, and T. Frank, "Surface-chemical studies of the mechanism of the direct synthesis of methylchlorosilanes," *Catalyzed Direct React. Silicon*, pp. 333–440, 1993.
- [25] W. Luo, G. Wang, and J. Wang, "Effect of CuCl particle size on the reduction reaction by silicon in preparation of contact mass used for methylchlorosilane synthesis," *Ind. Eng. Chem. Res.*, vol. 45, no. 1, pp. 129–133, 2006, doi: 10.1021/ie058044+.
- [26] J. Acker and K. Bohmhammel, "Thermodynamic assessment of the copper catalyzed direct synthesis of methylchlorosilanes," *J. Organomet. Chem.*, vol. 693, no. 15, pp. 2483–2493, Jul. 2008, doi: 10.1016/j.jorganchem.2008.04.026.
- [27] M. P. Clarke, "The direct synthesis of methylchlorosilanes," *J.*

- Organomet. Chem.*, vol. 376, no. 2–3, pp. 165–222, Nov. 1989, doi: 10.1016/0022-328X(89)85131-9.
- [28] C. Wang, G. Wang, and J. Wang, “A Bi-component Cu catalyst for the direct synthesis of methylchlorosilane from silicon and methyl chloride,” *Chinese J. Chem. Eng.*, vol. 22, no. 3, pp. 299–304, Mar. 2014, doi: 10.1016/S1004-9541(14)60034-3.
- [29] T. C. Frank and J. L. Falconer, “Silane formation on silicon: reaction kinetics and surface analysis,” *Langmuir*, vol. 1, no. 1, pp. 104–110, Jan. 1985, doi: 10.1021/la00061a017.
- [30] J. P. Agarwala and J. L. Falconer, “Kinetics of methylchlorosilane formation on Zn-promoted Cu₃Si,” *Int. J. Chem. Kinet.*, vol. 19, no. 6, pp. 519–537, 1987, doi: 10.1002/kin.550190605.
- [31] R. J. H. Voorhoeve and J. C. Vlugter, “Mechanism and kinetics of the metal-catalyzed synthesis of methylchlorosilanes. III. The catalytically active form of the copper catalyst,” *J. Catal.*, vol. 4, no. 2, pp. 123–133, Apr. 1965, doi: 10.1016/0021-9517(65)90003-5.
- [32] P. TRAMBOUZE, “CONTRIBUTION A LETUDE DU MECANISME DE LA SYNTHESE DES METHYCHLOROSILIANES,” *Bull. Soc. Chim. Fr.*, no. 11–1, pp. 1756–1765, 1956.
- [33] W. BANHOLZER, “Active site formation in the direct process for methylchlorosilanes,” *J. Catal.*, vol. 101, no. 2, pp. 405–415, Oct. 1986, doi: 10.1016/0021-9517(86)90268-X.
- [34] R. VOORHOEVE, “Mechanism and kinetics of the metal-

- catalyzed synthesis of methylchlorosilanes I. The synthesis of methylchlorosilanes in a fluid bed,” *J. Catal.*, vol. 3, no. 5, pp. 414–425, Oct. 1964, doi: 10.1016/0021-9517(64)90144-7.
- [35] R. VOORHOEVE, “Mechanism and kinetics of the metal-catalyzed synthesis of methylchlorosilanes II. The kinetics of the copper-catalyzed reaction of methyl chloride and silicon,” *J. Catal.*, vol. 4, no. 1, pp. 43–55, Feb. 1965, doi: 10.1016/0021-9517(65)90088-6.
- [36] C. Wang, T. Liu, Y. Huang, G. Wang, and J. Wang, “Promoter effects of Zn and Sn in the direct synthesis of methylchlorosilanes,” *Ind. Eng. Chem. Res.*, vol. 52, no. 15, pp. 5282–5286, Apr. 2013, doi: 10.1021/ie303515q.
- [37] V. D. KRYLOV and Y. N. EFREMOV, “THE STRUCTURE OF CU-SI ALLOYS AND THEIR CATALYTIC ACTIVITY IN THE REACTION WITH CHLORETHYL,” *ZHURNAL Fiz. KHIMII*, vol. 31, no. 11, pp. 2522-, 1957.
- [38] W. Luo, G. Wang, and J. Wang, “Surface morphology and catalytic activity of the contact mass in organosilane synthesis,” *Chem. Eng. Commun.*, vol. 193, no. 6, pp. 754–763, Jun. 2006, doi: 10.1080/00986440500267162.
- [39] J. M. Thomas, “Handbook Of Heterogeneous Catalysis. 2., completely revised and enlarged Edition. Vol. 1-8. Edited by G. Ertl, H. Knözinger, F. Schüth, and J. Weitkamp.,” *Angew. Chemie Int. Ed.*, vol. 48, no. 19, pp. 3390–3391, Apr. 2009, doi: 10.1002/anie.200901598.
- [40] G. Weber, N. Gourgoillon, D. Viale, B. Gillot, and P. Barret,

“Effect of small amounts of various additives on the reaction between a single crystal of silicon and fused copper chloride,” *React. Solids*, vol. 6, no. 1, pp. 75–93, 1988, doi: 10.1016/0168-7336(88)80047-0.

- [41] T. J. Wessel and D. G. Rethwisch, “Deactivation of CuSi and CuZnSnSi due to coke formation during the direct synthesis of methylchlorosilanes,” *J. Catal.*, vol. 161, no. 2, pp. 861–866, Jul. 1996, doi: 10.1006/jcat.1996.0248.
- [42] L. GASPERGALVIN, “Role of metallic promoters in the direct synthesis of methylchlorosilanes,” *J. Catal.*, vol. 128, no. 2, pp. 468–478, Apr. 1991, doi: 10.1016/0021-9517(91)90304-M.
- [43] W. F. Gilliam, “Preparation of Dialkyl-Substituted Dihalogenosilanes,” Feb. 1949.
- [44] C. H. Bartholomew, “Mechanisms of catalyst deactivation,” *Appl. Catal. A Gen.*, vol. 212, no. 1–2, pp. 17–60, Apr. 2001, doi: 10.1016/S0926-860X(00)00843-7.
- [45] J. B. Butt, “Catalyst Deactivation and Regeneration,” in *Catalysis: Science and Technology*, vol. 6, Hoboken, NJ, USA: John Wiley & Sons, Inc., 1984, pp. 1–63.
- [46] D. L. Trimm, “Deactivation and Regeneration,” in *Handbook of Heterogeneous Catalysis*, vol. 3–5, Weinheim, Germany: Wiley-VCH Verlag GmbH, 2008, pp. 1263–1282.
- [47] D. B. Dadyburjor, “Activation, deactivation, and poisoning of catalysts by John B. Butt and Eugene E. Petersen, Academic Press Inc., San Diego, 1988, 495 pp., \$95.00,” *AIChE J.*, vol. 35, no. 4,

- pp. 702–702, Apr. 1989, doi: 10.1002/aic.690350431.
- [48] P. G. Menon, “Coke on catalysts-harmful, harmless, invisible and beneficial types,” *J. Mol. Catal.*, vol. 59, no. 2, pp. 207–220, Apr. 1990, doi: 10.1016/0304-5102(90)85053-K.
- [49] M. Guisnet and P. Magnoux, “Organic chemistry of coke formation,” *Appl. Catal. A Gen.*, vol. 212, no. 1–2, pp. 83–96, Apr. 2001, doi: 10.1016/S0926-860X(00)00845-0.
- [50] I. Kiricsi, “Molecular Sieves: Science and Technology,” *Appl. Catal. A Gen.*, vol. 263, no. 1, p. 119, May 2004, doi: 10.1016/j.apcata.2004.02.007.
- [51] S. D. Jackson, *Catalysis: an integrated approach to homogeneous, heterogeneous, and industrial catalysis*, vol. 56, no. 2. Elsevier, 1995.
- [52] J. K. Nørskov, F. Studt, F. Abild-Pedersen, and T. Bligaard, “Heterogeneous Catalysis and a Sustainable Future,” in *Fundamental Concepts in Heterogeneous Catalysis*, Hoboken, NJ, USA: John Wiley & Sons, Inc, 2014, pp. 1–5.
- [53] “X-Ray Diffraction _ VEQTER _ Residual Stress Experts.” <http://www.veqter.co.uk/residual-stress-measurement/x-ray-diffraction> (accessed Aug. 03, 2020).
- [54] Y. Leng, *Materials characterization: Introduction to microscopic and spectroscopic methods: Second edition*. Weinheim, Germany: Wiley-VCH Verlag GmbH & Co. KGaA, 2013.
- [55] Π. Α. Ταραντίλης, “Φασματοσκοπία Raman (Raman Spectroscopy) Φασματοσκοπία Raman (Raman Spectroscopy

-),” *Encycl. Dict. Polym.*, vol. 14, p. 608, 1988.
- [56] N. Egeland, “Raman spectroscopy applied to enhanced oil recovery research.” 2015, doi: 10.13140/RG.2.1.3818.0322.
- [57] J. R. F. K. Nakamoto, *Introductory Raman Spectroscopy*. Elsevier, 1994.
- [58] E. Smith and G. Dent, *Modern Raman Spectroscopy - A Practical Approach*. Chichester, UK: John Wiley & Sons, Ltd, 2005.
- [59] M. S. Khopkar, “Basic Concepts Of Analytical Chemistry - S M Khopkar - Google Books,” 1998. [https://books.google.ca/books?id=e8Ju_n8DN1sC&pg=PA210&dq=beer%27s+law&hl=en&sa=X&redir_esc=y#v=onepage&q=beer's law&f=false](https://books.google.ca/books?id=e8Ju_n8DN1sC&pg=PA210&dq=beer%27s+law&hl=en&sa=X&redir_esc=y#v=onepage&q=beer's+law&f=false) (accessed Aug. 11, 2020).
- [60] J. D. Menczel and R. B. Prime, *Thermal Analysis of Polymers: Fundamentals and Applications*. Wiley, 2008.
- [61] P. Gabbott, *Principles and Applications of Thermal Analysis*. Oxford, UK: Blackwell Publishing Ltd, 2008.
- [62] S. R. Byrn, G. Zografis, and X. S. Chen, “Differential Scanning Calorimetry and Thermogravimetric Analysis,” in *Solid State Properties of Pharmaceutical Materials*, Hoboken: John Wiley & Sons, Inc., 2017, pp. 124–141.
- [63] C. Steiner, “Biochar: A Guide to Analytical Methods. By B.Singh, M.Camps-Arbestain & J.Lehmann (eds). Published by CRC Press, Boca Raton, FL, USA, 2017. ix + 320 pp, Paperback, £44.99 (ISBN 9781498765534),” *Soil Use Manag.*, vol. 34, no. 1, pp. 163–164, Mar. 2018, doi: 10.1111/sum.12389.

- [64] A. Boller, Y. Jin, and B. Wunderlich, "Heat capacity measurement by modulated DSC at constant temperature," *J. Therm. Anal.*, vol. 42, no. 2–3, pp. 307–330, Aug. 1994, doi: 10.1007/BF02548519.
- [65] P. J. Haines, M. Reading, and F. W. Wilburn, "Differential Thermal Analysis and Differential Scanning Calorimetry," in *Handbook of Thermal Analysis and Calorimetry*, vol. 1, Elsevier, 1998, pp. 279–361.
- [66] Z. Zhang *et al.*, "Facile solvothermal synthesis of porous cubic Cu microparticles as copper catalysts for Rochow reaction," *ACS Appl. Mater. Interfaces*, vol. 4, no. 3, pp. 1295–1302, Mar. 2012, doi: 10.1021/am3002605.
- [67] L. Fang, S. Dong, L. Shi, and Q. Sun, "Modification of $\text{CuCl}_2 \cdot 2\text{H}_2\text{O}$ by dielectric barrier discharge and its application in the hydroxylation of benzene," *New J. Chem.*, vol. 43, no. 32, pp. 12744–12753, 2019, doi: 10.1039/C9NJ03261D.
- [68] X. Sun, X. Zhang, X. Cao, and X. Zhao, "Optimization of reaction conditions for cyclohexane to cyclohexanone with *t*-butylhydroperoxide over CuCl_2 loaded with activated carbon," *J. Braz. Chem. Soc.*, vol. 27, no. 1, pp. 202–208, Jan. 2016, doi: 10.5935/0103-5053.20150271.
- [69] M. Chmielová, J. Seidlerová, and Z. Weiss, "X-ray diffraction phase analysis of crystalline copper corrosion products after treatment in different chloride solutions," *Corros. Sci.*, vol. 45, no. 5, pp. 883–889, May 2003, doi: 10.1016/S0010-938X(02)00176-2.

- [70] M. Ferrandon, M. Lewis, D. Tatterson, and A. Zdunek, "Status of the development effort for the thermochemical Cu-Cl cycle," 2008.
- [71] "United States Patent (19) Pastor (54) METHOD FOR PREPARING CUPRIC," Dec. 24, 1984.
- [72] A. Wang, M. Zhang, H. Yin, S. Liu, M. Liu, and T. Hu, "Direct reaction between silicon and methanol over Cu-based catalysts: Investigation of active species and regeneration of CuCl catalyst," *RSC Adv.*, vol. 8, no. 34, pp. 19317–19325, May 2018, doi: 10.1039/c8ra03125h.
- [73] I. Muhammad, N. Makwashi, and G. Manos, "Catalytic degradation of linear low-density polyethylene over HY-zeolite via pre-degradation method," *J. Anal. Appl. Pyrolysis*, vol. 138, pp. 10–21, Mar. 2019, doi: 10.1016/j.jaap.2018.11.025.
- [74] D. Starodub, E. P. Gusev, E. Garfunkel, and T. Gustafsson, "Silicon oxide decomposition and desorption during the thermal oxidation of silicon," *Surf. Rev. Lett.*, vol. 6, no. 1, pp. 45–52, Feb. 1999, doi: 10.1142/S0218625X99000081.
- [75] G. De Micco, A. E. Bohé, and D. M. Pasquevich, "A thermogravimetric study of copper chlorination," *J. Alloys Compd.*, vol. 437, no. 1–2, pp. 351–359, Jun. 2007, doi: 10.1016/j.jallcom.2006.08.003.
- [76] M. Guido, G. Balducci, G. Gigli, and M. Spoliti, "Mass spectrometric study of the vaporization of cuprous chloride and the dissociation energy of Cu₃Cl₃, Cu₄Cl₄, and Cu₅Cl₅," *J. Chem. Phys.*, vol. 55, no. 9, pp. 4566–4572, Nov. 1971, doi:

10.1063/1.1676790.

- [77] K. Uchinokura, T. Sekine, and E. Matsuura, "Raman scattering by silicon," *Solid State Commun.*, vol. 11, no. 1, pp. 47–49, Jul. 1972, doi: 10.1016/0038-1098(72)91127-1.
- [78] B. Graczykowski *et al.*, "Thermal conductivity and air-mediated losses in periodic porous silicon membranes at high temperatures," *Nat. Commun.*, vol. 8, no. 1, pp. 1–9, Dec. 2017, doi: 10.1038/s41467-017-00115-4.
- [79] A. Ferrari and J. Robertson, "Interpretation of Raman spectra of disordered and amorphous carbon," *Phys. Rev. B - Condens. Matter Mater. Phys.*, vol. 61, no. 20, pp. 14095–14107, May 2000, doi: 10.1103/PhysRevB.61.14095.
- [80] M. Raffi *et al.*, "Investigations into the antibacterial behavior of copper nanoparticles against Escherichia coli," *Ann. Microbiol.*, vol. 60, no. 1, pp. 75–80, Mar. 2010, doi: 10.1007/s13213-010-0015-6.
- [81] H. Liu *et al.*, "Diffusion-controlled synthesis of Cu-based for the Rochow reaction," *Sci. China Mater.*, vol. 60, no. 12, pp. 1215–1226, Dec. 2017, doi: 10.1007/s40843-017-9128-4.
- [82] M. Chen *et al.*, "Urchin-like ZnO microspheres synthesized by thermal decomposition of hydrozincite as a copper catalyst promoter for the Rochow reaction," *RSC Adv.*, vol. 2, no. 10, pp. 4164–4168, May 2012, doi: 10.1039/c2ra01022d.
- [83] S. Zou *et al.*, "Novel leaflike Cu-O-Sn nanosheets as highly efficient catalysts for the Rochow reaction," *J. Catal.*, vol. 337,

- pp. 1–13, May 2016, doi: 10.1016/j.jcat.2016.01.009.
- [84] G. Weber, D. Viale, H. Souha, B. Gillot, and P. Barret, “Kinetic data and mechanistic model for the reaction between Si and CuCl,” *Solid State Ionics*, vol. 32–33, no. PART 1, pp. 250–257, Feb. 1989, doi: 10.1016/0167-2738(89)90229-4.
- [85] L. Caillod, G. Bergeret, J. C. Bertolini, C. Garcia-Escomel, and P. Colin, “Comparison of Cu₃Si and Cu₅Si reactivities in direct synthesis of dimethyldichlorosilane,” pp. 133–145, 2006.
- [86] H. Liu *et al.*, “Converting industrial waste contact masses into effective multicomponent copper-based catalysts for the Rochow process,” *Particuology*, vol. 37, pp. 1–8, Apr. 2018, doi: 10.1016/j.partic.2017.05.008.
- [87] TUINSTR A F and KOENIG JL, “RAMAN SPECTRUM OF GRAPHITE,” *J. Chem. Phys.*, vol. 53, no. 3, pp. 1126–1130, Aug. 1970, doi: 10.1063/1.1674108.
- [88] R. J. Nemanich and S. A. Solin, “First- and second-order Raman scattering from finite-size crystals of graphite,” *Phys. Rev. B*, vol. 20, no. 2, pp. 392–401, Jul. 1979, doi: 10.1103/PhysRevB.20.392.
- [89] D. Espinat *et al.*, “Characterization of the coke formed on reforming catalysts by laser raman spectroscopy,” *Appl. Catal.*, vol. 16, no. 3, pp. 343–354, Jun. 1985, doi: 10.1016/S0166-9834(00)84398-5.
- [90] C. Beny-Bassez and J. N. Rouzaud, “Characterization of Carbonaceous Materials By Correlated Electron and Optical Microscopy and Raman Microspectroscopy.,” *Scan. Electron*

Microsc., no. pt 1, pp. 119–132, 1985.

- [91] J. Dill and B. Wopenka, “BUIIETIII DE TASSOCIATIOTTI MINERALOGIOUE DU CAIADA rHE CAJIADIAJI JOURNAT OF THE MTNERAIOGICAT ASSOCIATIOII| OF CAIIADA RAMAN SPECTRA OF GRAPHITE AS INDICATORS OF DEGREE OF METAMORPHISM,” 1991.
- [92] B. M. Vogelaar, A. D. van Langeveld, S. Eijsbouts, and J. A. Moulijn, “Analysis of coke deposition profiles in commercial spent hydroprocessing catalysts using Raman spectroscopy,” *Fuel*, vol. 86, no. 7–8, pp. 1122–1129, May 2007, doi: 10.1016/j.fuel.2006.10.002.
- [93] Y. Xie, J. You, L. Lu, M. Wang, and J. Wang, “Raman Spectroscopic Study of Coal Samples during Heating,” *Appl. Sci.*, vol. 9, no. 21, p. 4699, Nov. 2019, doi: 10.3390/app9214699.
- [94] T. Jawhari, P. J. Hendra, H. A. Willis, and M. Judkins, “Quantitative analysis using Raman methods,” *Spectrochim. Acta Part A Mol. Spectrosc.*, vol. 46, no. 2, pp. 161–170, Jan. 1990, doi: 10.1016/0584-8539(90)80086-E.
- [95] A. C. Selden, “Raman Spectroscopy of Gases and Liquids,” *Opt. Acta Int. J. Opt.*, vol. 26, no. 10, pp. 1239–1240, Oct. 1979, doi: 10.1080/713819897.
- [96] W. Weng *et al.*, “Flexible and stable lithium ion batteries based on three-dimensional aligned carbon nanotube/silicon hybrid electrodes,” *J. Mater. Chem. A*, vol. 2, no. 24, p. 9306, 2014, doi: 10.1039/c4ta00711e.

- [97] J. Yang, A. Kraysberg, and Y. Ein-Eli, “In-situ Raman spectroscopy mapping of Si based anode material lithiation,” *J. Power Sources*, vol. 282, pp. 294–298, May 2015, doi: 10.1016/j.jpowsour.2015.02.044.
- [98] O. Beyssac, B. Goffé, C. Chopin, and J. N. Rouzaud, “Raman spectra of carbonaceous material in metasediments: a new geothermometer,” *J. Metamorph. Geol.*, vol. 20, no. 9, pp. 859–871, Dec. 2002, doi: 10.1046/j.1525-1314.2002.00408.x.
- [99] O. Beyssac, B. Goffé, J.-P. Petitet, E. Froigneux, M. Moreau, and J.-N. Rouzaud, “On the characterization of disordered and heterogeneous carbonaceous materials by Raman spectroscopy,” *Spectrochim. Acta Part A Mol. Biomol. Spectrosc.*, vol. 59, no. 10, pp. 2267–2276, Aug. 2003, doi: 10.1016/S1386-1425(03)00070-2.
- [100] B. Guichard, M. Roy-Auberger, E. Devers, B. Rebours, A. A. Quoineaud, and M. Digne, “Characterization of aged hydrotreating catalysts. Part I: Coke depositions, study on the chemical nature and environment,” *Appl. Catal. A Gen.*, vol. 367, no. 1–2, pp. 1–8, Oct. 2009, doi: 10.1016/j.apcata.2009.07.024.
- [101] S. R. Bare *et al.*, “Characterization of Coke on a Pt-Re/ γ -Al₂O₃ Re-Forming Catalyst: Experimental and Theoretical Study,” *ACS Catal.*, vol. 7, no. 2, pp. 1452–1461, Feb. 2017, doi: 10.1021/acscatal.6b02785.
- [102] N. Souza *et al.*, “Upcycling spent petroleum cracking catalyst: Pulsed laser deposition of single-wall carbon nanotubes and silica nanowires,” *RSC Adv.*, vol. 6, no. 76, pp. 72596–72606, Jul. 2016,

doi: 10.1039/c6ra15479d.

- [103] C. Brolly, J. Parnell, and S. Bowden, “Raman spectroscopy: Caution when interpreting organic carbon from oxidising environments,” *Planet. Space Sci.*, vol. 121, pp. 53–59, Feb. 2016, doi: 10.1016/j.pss.2015.12.008.
- [104] B. Kwiecinska, I. Suárez-Ruiz, C. Paluszkiewicz, and S. Rodrigues, “Raman spectroscopy of selected carbonaceous samples,” *Int. J. Coal Geol.*, vol. 84, no. 3–4, pp. 206–212, Dec. 2010, doi: 10.1016/j.coal.2010.08.010.
- [105] F. Menges, *Spectroscopy Ninja presents: SPECTRAGRYPH*. 2017.
- [106] R. A. DiLeo, B. J. Landi, and R. P. Raffaele, “Purity assessment of multiwalled carbon nanotubes by Raman spectroscopy,” *J. Appl. Phys.*, vol. 101, no. 6, p. 064307, Mar. 2007, doi: 10.1063/1.2712152.
- [107] G. Maes, “Handbook of Raman Spectroscopy. From the Research Laboratory to the Process Line,” *Spectrochim. Acta Part A Mol. Biomol. Spectrosc.*, vol. 59, no. 1, p. 211, Jan. 2003, doi: 10.1016/S1386-1425(02)00113-0.
- [108] J. Schwan, S. Ulrich, V. Batori, H. Ehrhardt, and S. R. P. Silva, “Raman spectroscopy on amorphous carbon films,” *J. Appl. Phys.*, vol. 80, no. 1, pp. 440–447, Jul. 1996, doi: 10.1063/1.362745.
- [109] X. Wu, W. Zhang, Z. Li, Y. Zhang, S. Huang, and Q. Liu, “Effects of various methylchlorosilanes on physicochemical properties of

- ambient pressure dried silica aerogels,” *J. Nanoparticle Res.*, vol. 21, no. 11, p. 234, Nov. 2019, doi: 10.1007/s11051-019-4685-0.
- [110] Z. Li, X. Cheng, S. He, X. Shi, and H. Yang, “Characteristics of ambient-pressure-dried aerogels synthesized via different surface modification methods,” *J. Sol-Gel Sci. Technol.*, vol. 76, no. 1, pp. 138–149, Oct. 2015, doi: 10.1007/s10971-015-3760-y.
- [111] M. Wolf, N. Raman, N. Taccardi, M. Haumann, and P. Wasserscheid, “Coke Formation during Propane Dehydrogenation over Ga–Rh Supported Catalytically Active Liquid Metal Solutions,” *ChemCatChem*, vol. 12, no. 4, pp. 1085–1094, Feb. 2020, doi: 10.1002/cctc.201901922.
- [112] S. He, C. Sun, X. Yang, B. Wang, X. Dai, and Z. Bai, “Characterization of coke deposited on spent catalysts for long-chain-paraffin dehydrogenation,” *Chem. Eng. J.*, vol. 163, no. 3, pp. 389–394, Oct. 2010, doi: 10.1016/j.cej.2010.07.024.
- [113] L. Bokobza and J. Zhang, “Raman spectroscopic characterization of multiwall carbon nanotubes and of composites,” *Express Polym. Lett.*, vol. 6, no. 7, pp. 601–608, Jul. 2012, doi: 10.3144/expresspolymlett.2012.63.
- [114] Y. Zhang *et al.*, “Morphology-dependent catalytic properties of nanocupric oxides in the Rochow reaction,” *Nano Res.*, vol. 11, no. 2, pp. 804–819, Feb. 2018, doi: 10.1007/s12274-017-1689-x.
- [115] P. Zhou, “Choosing the Most Suitable Laser Wavelength For Your Raman Application,” 2015.

Appendix A.

A.1 Raman Spectroscopy Results

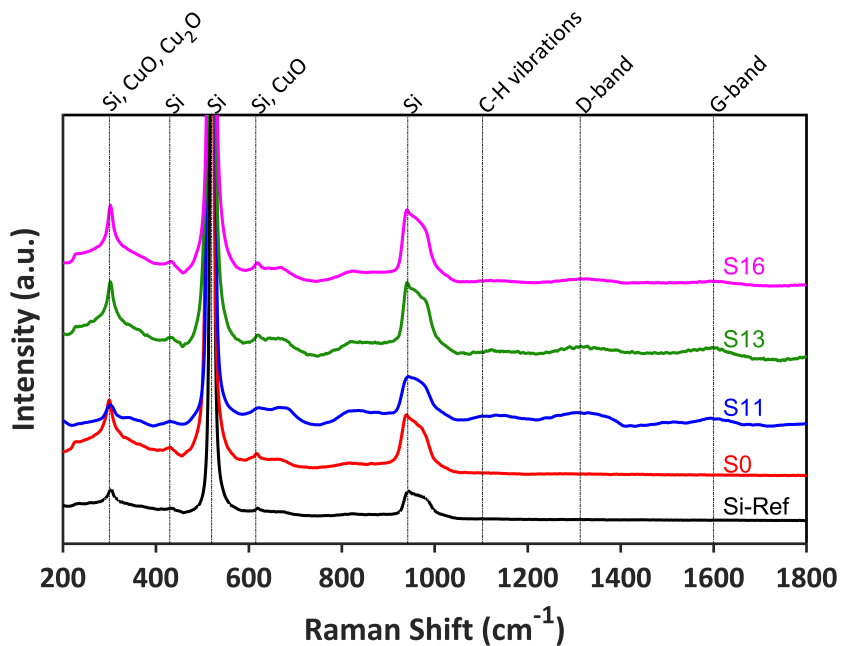


Figure A.1: Raman spectra of Si-Ref, S0, S11, S13 and S16 samples. S11, S13, and S16 spectra are measured at silicon rich spots. Measured with 632 nm laser from Raman shift of 200 cm^{-1} to 1800 cm^{-1} .

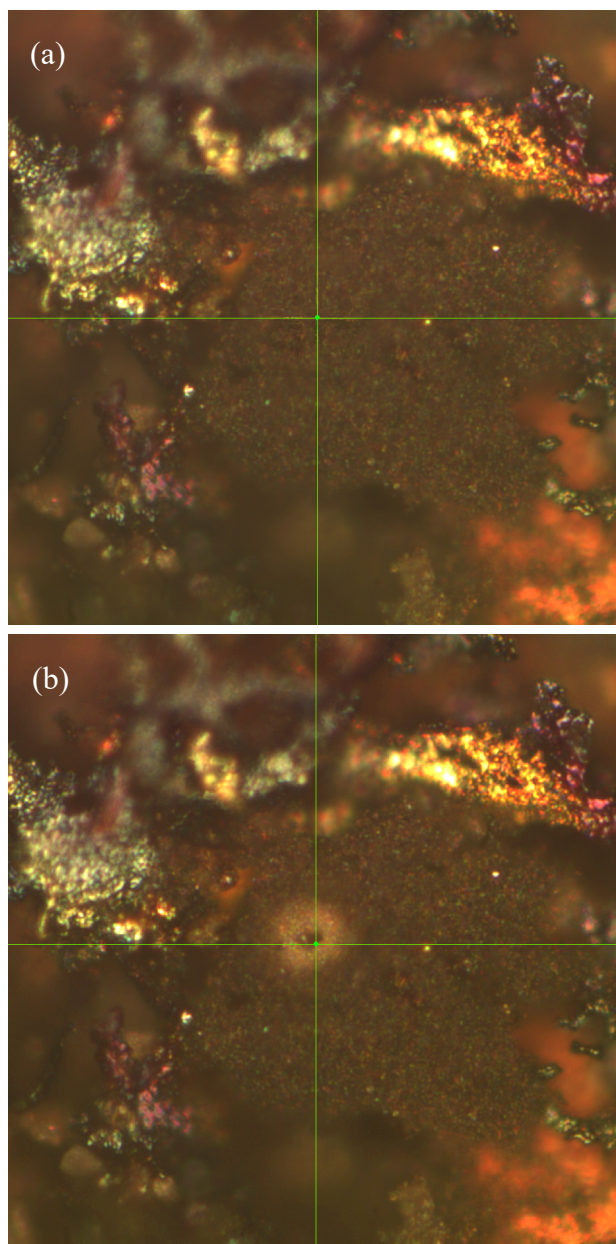


Figure A.2: Microscope image of S19 sample showing coke oxidation under Raman laser of 633 nm wavelength. (a) Microscope image before exposure to laser (b) Microscope image of same spot after 5 minutes of exposure to laser.

A.2 Thermal Analysis Results

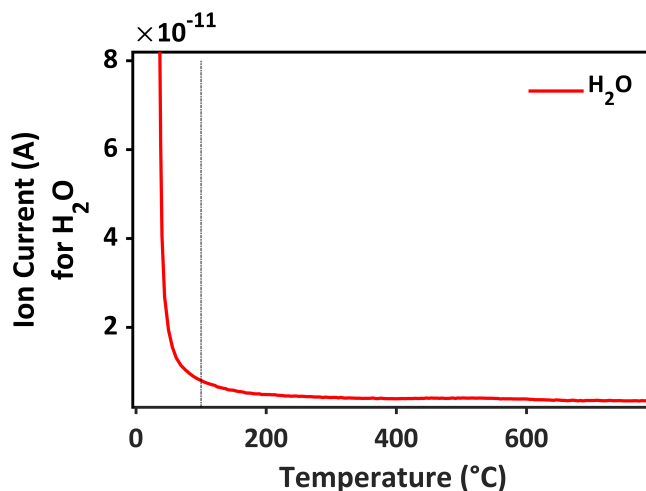


Figure A.3: Mass spectroscopic analysis of Si-Ref sample in oxidative atmosphere (55 mL/min air and 25 mL/min argon) from 35 °C to 800 °C at 10 °C/min heating rate.

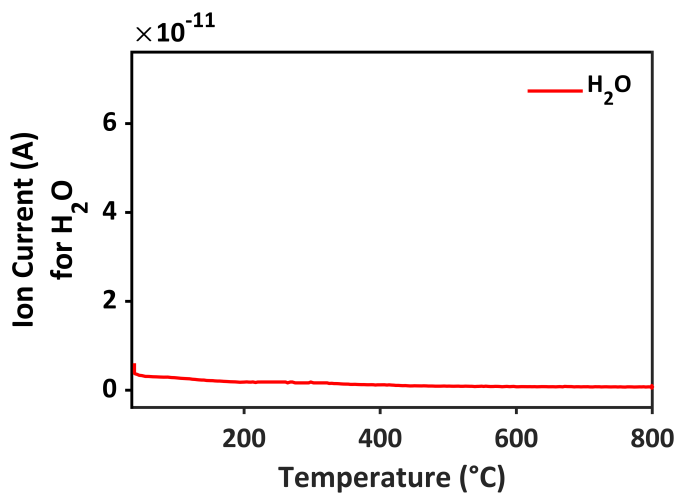


Figure A.4: Mass spectroscopic analysis of CuCl sample in oxidative atmosphere (55 mL/min air and 25 mL/min argon) from 35 °C to 800 °C at 10 °C/min heating rate.

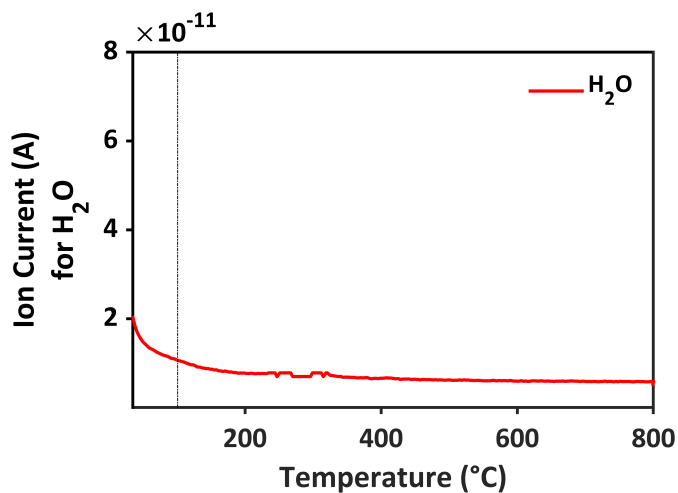


Figure A.5: Mass spectroscopic analysis of CuCl sample in inert atmosphere (80 mL/min argon) from 35 °C to 800 °C at 10 °C/min heating rate.

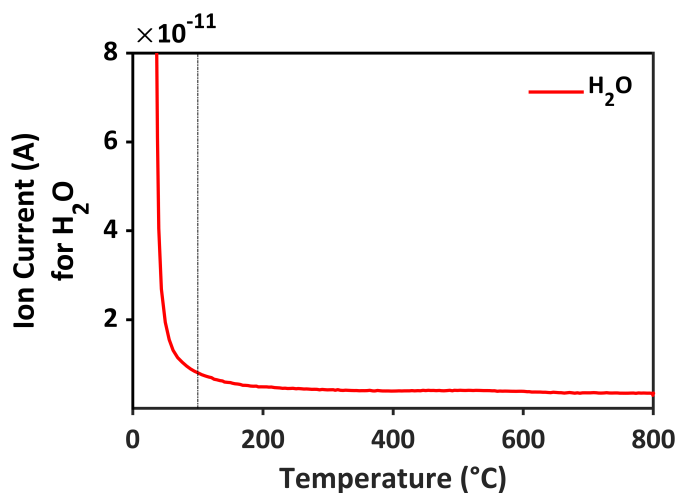


Figure A.6: Mass spectroscopic analysis of S0 sample in oxidative atmosphere (55 mL/min air and 25 mL/min argon) from 35 °C to 800 °C at 10 °C/min heating rate.

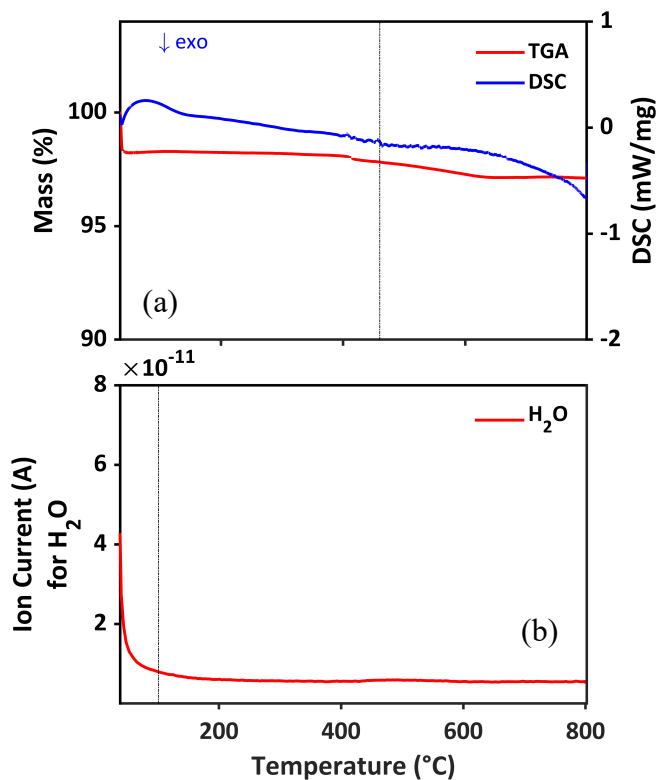


Figure A.7: TGA, DSC and MS analysis of S0 in inert atmosphere (80 mL/min argon) from 35 °C to 800 °C at 10 °C/min heating rate. (a) TGA curve on the left and DSC curve on the right (b) MS ion current for H₂O ($m/z=18$)

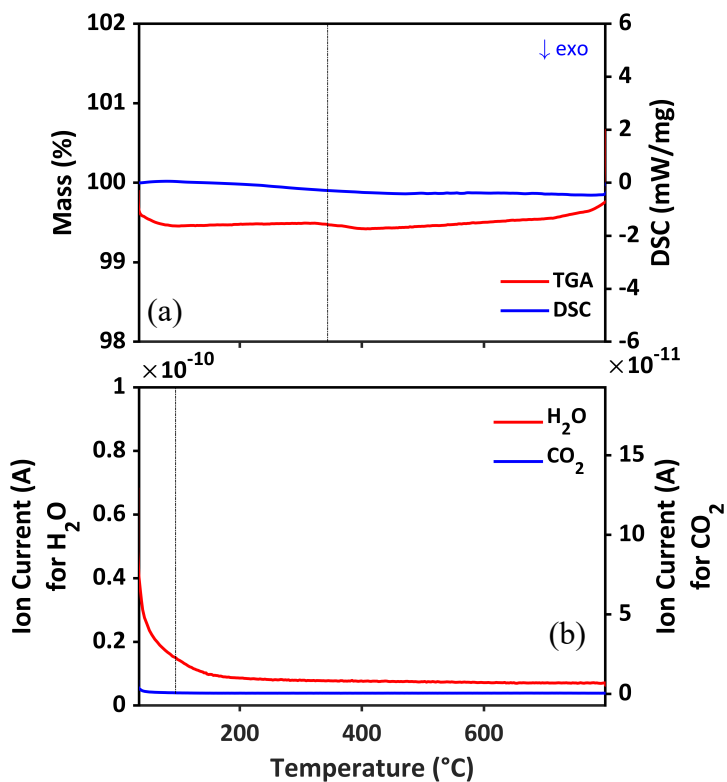


Figure A.8: TGA, DSC and MS analysis of S11 in inert atmosphere (80 mL/min argon) from 35 °C to 800 °C at 10 °C/min heating rate. (a) TGA curve on the left and DSC curve on the right (b) MS ion current for H₂O ($m/z=18$) on the left and CO₂ ($m/z=44$) on the right.

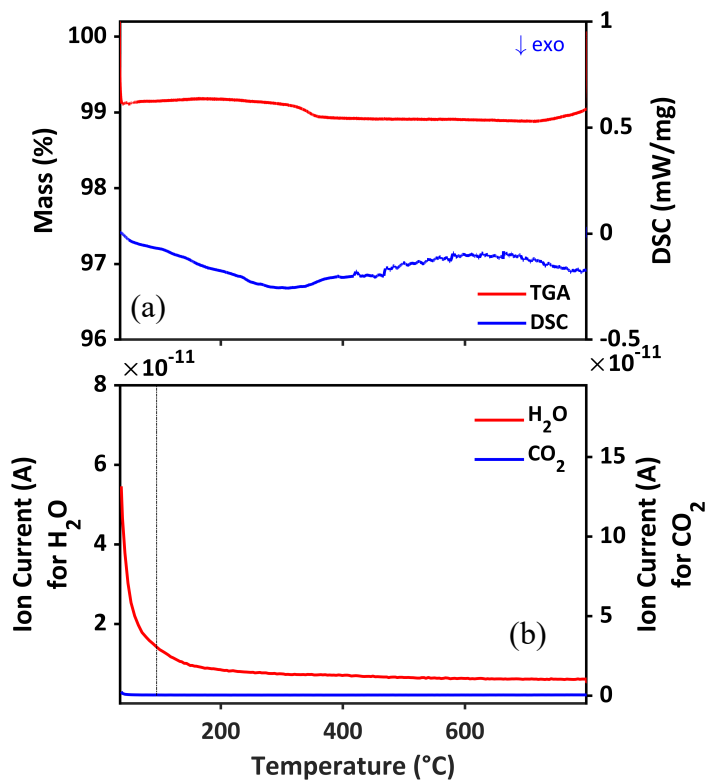


Figure A.9: TGA, DSC and MS analysis of S15 in inert atmosphere (80 mL/min argon) from 35 °C to 800 °C at 10 °C/min heating rate. **(a)** TGA curve on the left and DSC curve on the right **(b)** MS ion current for H₂O ($m/z=18$) on the left and CO₂ ($m/z=44$) on the right.

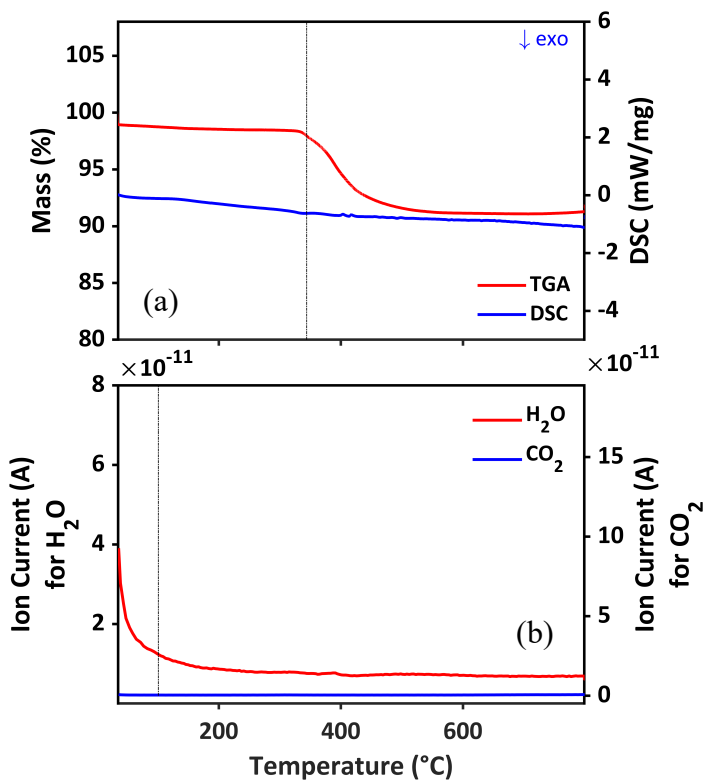


Figure A.10: TGA, DSC and MS of S17 in inert atmosphere (80 mL/min argon) from 35 °C to 800 °C at 10 °C/min heating rate. (a) TGA curve on the left and DSC curve on the right. Mass loss at around 400 °C is attributed to CuCl decomposition. (b) MS ion current for H₂O ($m/z=18$) on the left and CO₂ ($m/z=44$) on the right.

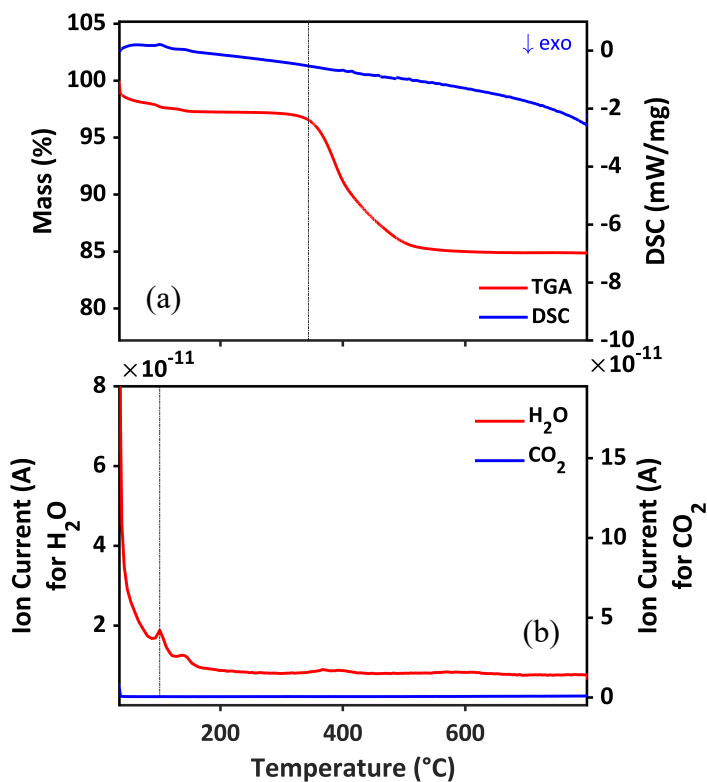


Figure A.11: TGA, DSC and MS analysis of S19 in inert atmosphere (80 mL/min argon) from 35 °C to 800 °C at 10 K/min heating rate. (a) TGA curve on the left and DSC curve on the right. Mass loss at around 400 °C is attributed to CuCl decomposition. (b) MS ion current for H₂O ($m/z=18$) on the left and CO₂ ($m/z=44$) on the right.

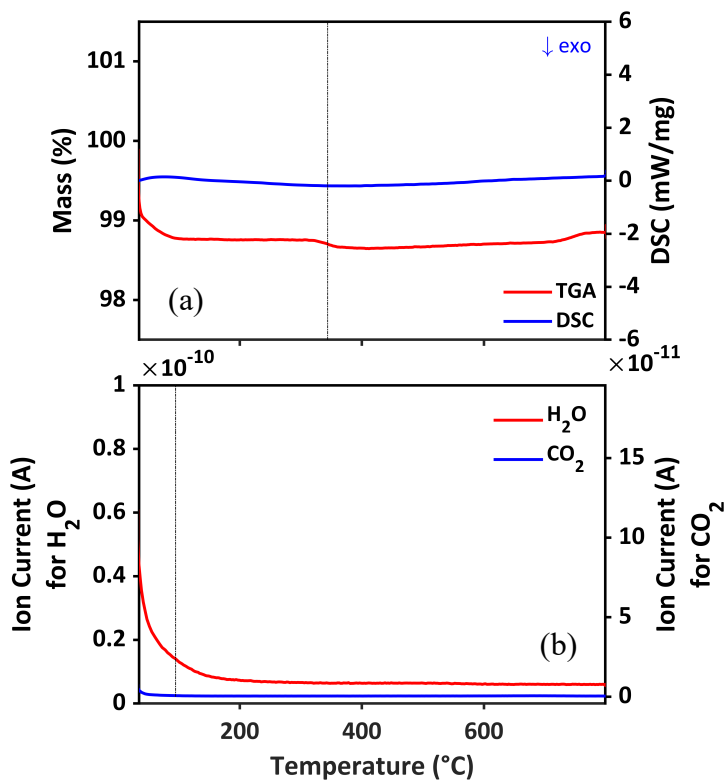


Figure A.12: TGA, DSC and MS analysis of S12 in inert atmosphere (80 mL/min argon) from 35 °C to 800 °C at 10 K/min heating rate. **(a)** TGA curve on the left and DSC curve on the right. Mass loss at around 400 °C is attributed to CuCl decomposition. **(b)** MS ion current for H₂O ($m/z=18$) on the left and CO₂ ($m/z=44$) on the right.

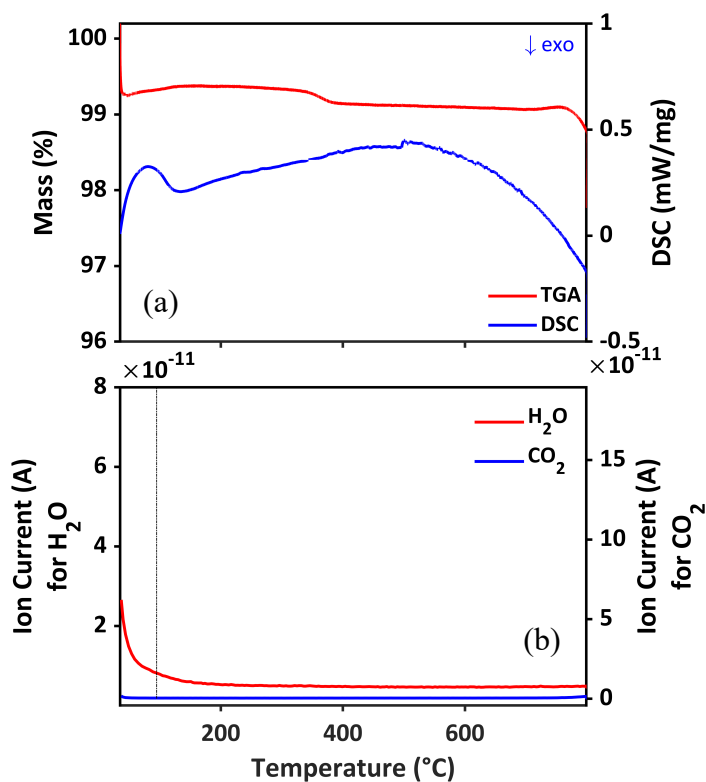


Figure A.13: TGA, DSC and MS analysis of S16 in inert atmosphere (80 mL/min argon) from 35 °C to 800 °C at 10 K/min heating rate. (a) TGA curve on the left and DSC curve on the right. Mass loss at around 400 °C is attributed to CuCl decomposition. (b) MS ion current for H₂O ($m/z=18$) on the left and CO₂ ($m/z=44$) on the right.

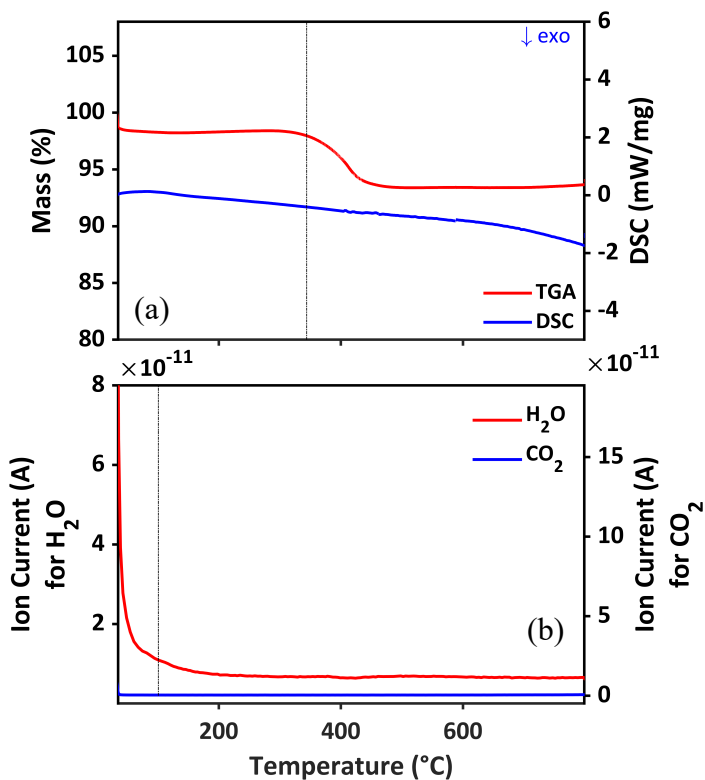


Figure A.14: TGA/MS analysis of S18 in inert atmosphere (80 mL/min argon) from 35 °C to 800 °C at 10 °C/min heating rate. **(a)** TGA curve on the left and DSC curve on the right. Mass loss at around 400 °C is attributed to CuCl decomposition. **(b)** MS ion current for H₂O ($m/z=18$) on the left and CO₂ ($m/z=44$) on the

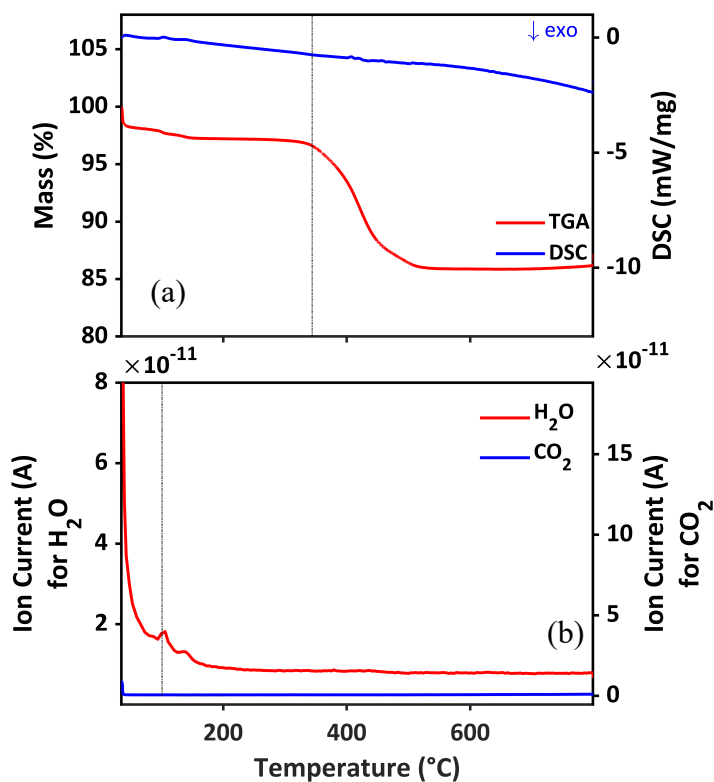


Figure A.15: TGA, DSC and MS analysis of S20 in inert atmosphere (80 mL/min argon) from 35 °C to 800 °C at 10 K/min heating rate. (a) TGA curve on the left and DSC curve on the right. Mass loss at around 420 °C is attributed to CuCl decomposition. (b) MS ion current for H₂O ($m/z=18$) on the left and CO₂ ($m/z=44$) on the right.

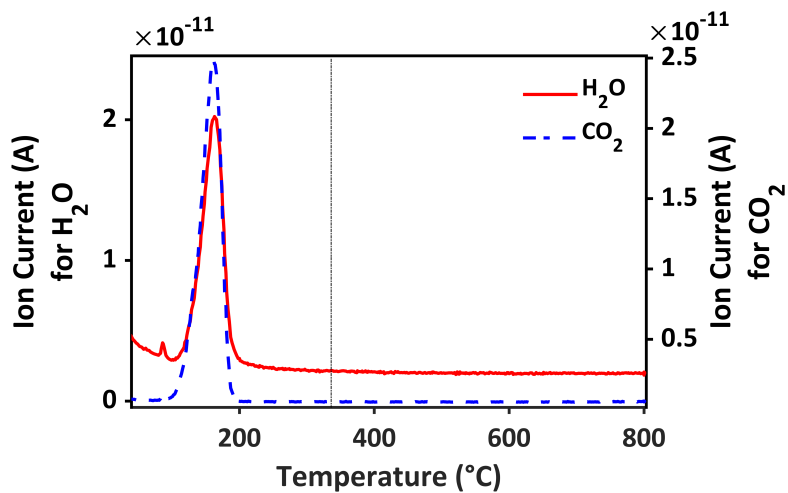


Figure A.16: Mass spectrometry result of NaHCO₃ in oxidative atmosphere (55 ml/min air and 25 ml/min argon) from 35 °C to 800 °C at 10 K/min heating rate. H₂O ($m/z=18$) on the left and CO₂ ($m/z=44$) on the right.

Appendix B

B.1 Risk Assessment



Detailed Risk Report

ID	34532	Status	Date
Risk Area	Risikovurdering: Helse, miljø og sikkerhet (HMS)	Created	03.09.2019
Created by	Hammad Farooq	Assessment started	03.09.2019
Responsible	Hammad Farooq	Measures decided	
		Closed	

**Risk Assessment:****CAT, Master student, 2019, Hammad Farooq****Valid from-to date:**

9/3/2019 - 8/31/2020

Location:

Gløshaugen, Kjemi Blok 5 (K5)

Goal / purpose

Risk assessment of my thesis work as a Master's student: "Effect of CuCl and Zn on the Cu₃Si Formation and Coke Deposition in the Direct Synthesis of Dimethyldichlorosilane".

Background

International master's student

Description and limitations

- The use of thermogravimetric analysis (TGA) to study and analyze the mass change with temperature. Heating up the samples in the range of 30-800 degrees celsius. Using synthetic air and protective argon gases at atmospheric pressure for a duration of almost 3 hours for each run.
- Raman Spectroscopy to determine the degree of order of the carbon species present in the samples. Ex-situ experiment using the 633 nm visible laser.
- X-ray diffraction analysis to determine the crystalline structure.

>>>April-May-June 2020 - preventive measures towards Covid-situation:

- 1) Switch off procedure for Soxhlet Extraction in Lab 317
 - Soxhlet extraction is a continual process that can be run 24 hrs without any oversight. Maximum temperature would be upto 200 °C.
 - Equipment can be shutdown by just turning off the heater, either from on-board power button or by plugging off the power cord.
 - As an extra measure, cooling water should be kept on, after shutting down the heater.
- 2) Extra-safety measurements in the lab
 - No toxic gases are involved in the process. Some organic solvents (Dichloromethane) have a low boiling point.
 - Soxhlet extraction is semi-closed system. If the cooling water is kept ON, chances of fumes formation are low to none.
- 3) Safety measures related to spread of covid19 infection:
 - Avoid touching the face
 - Disinfection before and after with ethanol on all surfaces you are in contact with (door knob – card reader with code panel)
 - Keep 2m distance from colleagues
 - Use nitrile gloves when touching shared lab set-ups and equipment
 - Wash hands as often as possible

Prerequisites, assumptions and simplifications

- HSE training
- Training for TGA (lab K5 441)
- Training for Raman (lab K5 427)
- Training for XRD (K2-113)

Attachments

apparatus card.pdf

References

[Ingen registreringer]



Summary, result and final evaluation

The summary presents an overview of hazards and incidents, in addition to risk result for each consequence area.

Hazard:	Chemicals used			
Incident:	Contact with Silicon powder when handling samples provided by Elkem			
Consequence area:	Helse	Risk before measures:	Risiko after measures:	
	Ytre miljø	Risk before measures:	Risiko after measures:	
Hazard:	Laser class 3 in Raman spectroscopy			
Incident:	Eye injury			
Consequence area:	Helse	Risk before measures:	Risiko after measures:	
Hazard:	Exposure to X-rays in XRD lab			
Incident:	Skin burn			
Consequence area:	Helse	Risk before measures:	Risiko after measures:	
Hazard:	High temperature of upto 800°C in TGA experiment			
Incident:	Hand burn			
Consequence area:	Helse	Risk before measures:	Risiko after measures:	
Hazard:	Pressurized gas (air and/or inter gas)			
Incident:	Gas leak			
Consequence area:	Helse	Risk before measures:	Risiko after measures:	
	Materielle verdier	Risk before measures:	Risiko after measures:	




Hazard: Working in the lab under covid-situation

Incident: Contact with commonly used glass equipment

Consequence area: Helse

Risk before
measures:

 Risiko after
measures:



Final evaluation



Organizational units and people involved

A risk assessment may apply to one or more organizational units, and involve several people. These are listed below.

Organizational units which this risk assessment applies to

- Institutt for kjemisk prosesssteknologi

Participants

Readers

Mehdi Mahmoodinia
 Estelle Marie M. Vanhaecke
 Hilde Johnsen Venvik
 Kristin Høydalsvik Wells
 Zhenping Cai
 Jens Norrman
 Edd Anders Blekkan

Others involved/stakeholders

[Ingen registreringer]

The following accept criteria have been decided for the risk area Risikovurdering: Helse, miljø og sikkerhet (HMS):





Overview of existing relevant measures which have been taken into account

The table below presents existing measures which have been taken into account when assessing the likelihood and consequence of relevant incidents.

Hazard	Incident	Measures taken into account
Chemicals used	Contact with Silicon powder when handling samples provided by Elkem	Safety goggles
	Contact with Silicon powder when handling samples provided by Elkem	Lab gloves
	Contact with Silicon powder when handling samples provided by Elkem	Safety goggles
	Contact with Silicon powder when handling samples provided by Elkem	Lab gloves
Laser class 3 in Raman spectroscopy	Eye injury	Safety goggles
	Eye injury	Safety goggles
Exposure to X-rays in XRD lab	Skin burn	Safety goggles
	Skin burn	Lab gloves
	Skin burn	Safety goggles
	Skin burn	Lab gloves
High temperature of upto 800°C in TGA experiment	Hand burn	Lab gloves
	Hand burn	Safety goggles
	Hand burn	Lab gloves
Pressurized gas (air and/or inter gas)	Gas leak	Gas detectors
	Gas leak	Gas detectors
Working in the lab under covid-situation	Contact with commonly used glass equipment	Safety goggles
	Contact with commonly used glass equipment	Lab gloves
	Contact with commonly used glass equipment	Disinfection with Ethanol
	Contact with commonly used glass equipment	Disinfection with Ethanol
	Contact with commonly used glass equipment	Apparatus Card

Existing relevant measures with descriptions:

Safety goggles

When handling silicon powder samples or performing Raman spectroscopy, safety goggles are mandatory.

Lab gloves

[Ingen registreringer]

Gas detectors

[Ingen registreringer]



Lab coat

[Ingen registreringer]

Disinfection with Ethanol

Commonly used glass equipments should be washed and disinfected with ethanol before and after use.

Apparatus Card

Apparatus card has been signed by my supervisor and pasted on the fumehood in Lab317.



Risk analysis with evaluation of likelihood and consequence

This part of the report presents detailed documentation of hazards, incidents and causes which have been evaluated. A summary of hazards and associated incidents is listed at the beginning.

The following hazards and incidents has been evaluated in this risk assessment:

- **Chemicals used**
 - Contact with Silicon powder when handling samples provided by Elkem
- **Laser class 3 in Raman spectroscopy**
 - Eye injury
- **Exposure to X-rays in XRD lab**
 - Skin burn
- **High temperature of upto 800°C in TGA experiment**
 - Hand burn
- **Pressurized gas (air and/or inter gas)**
 - Gas leak
- **Working in the lab under covid-situation**
 - Contact with commonly used glass equipment



Detailed view of hazards and incidents:

Hazard: Chemicals used

Risk involved in handling of the chemicals being used

Incident: Contact with Silicon powder when handling samples provided by Elkem

Any exposure to silicon powder can cause irritation to skin.

Cause: Improper handling

Description:

Improper handling of silicon powder can be hazardous to skin and environment.

Likelihood of the incident (common to all consequence areas): **Less likely (2)**

Kommentar:

Lab gloves and goggles are available in the lab and mandatory to use.

Consequence area: Helse

Assessed consequence: **Medium (2)**

Comment: Exposure to silicon may lead to reddening of skin, but with use of safety goggles and lab gloves, the consequences are not high.

Risk:



Consequence area: Ytre miljø

Assessed consequence: **Small (1)**

Comment: If silicon powder is handled carefully, the chances of any incident are minute.

Risk:





Hazard: Laser class 3 in Raman spectroscopy

Exposure to class 3 laser in Raman-IR (K5.427).

Incident: Eye injury

Class 3 lasers are hazardous for eye exposure and may cause burns to the retina.

Cause: Direct contact with laser

Description:

If the laser beam is directed towards someone's eyes, it can cause damage to retina.

Likelihood of the incident (common to all consequence areas): **Unlikely (1)**

Kommentar:

Knowledge and training of Raman IR along with use of PPE (safety goggles) reduces the likelihood.

Consequence area: Helse

Assessed consequence: **Medium (2)**

Comment: Exposure to class 3 laser is considered to be relatively less dangerous when using proper PPE.

Risk:





Hazard: Exposure to X-rays in XRD lab

When performing XRD analysis, exposure to x-rays may be caused by leakage of primary beam through cracks in shielding.

Incident: Skin burn

Exposure to x-rays from primary beam can cause reddening of skin and skin burn.

Cause: Cracks in shielding

Description:

If there are cracks in the shielding, primary beam may leak through.

Likelihood of the incident (common to all consequence areas): **Less likely (2)**

Kommentar:

Lab training is provided and PPE (safety goggles and lab gloves) are mandatory to wear when working in the lab.

Consequence area: Helse

Assessed consequence: **Medium (2)**

Comment: Exposure to leaked rays can cause skin burn.

Risk:




Hazard: High temperature of upto 800°C in TGA experiment

During thermal gravimetric analysis of the samples, temperature rises upto 800°C.

Incident: Hand burn

Handling of crucible before TGA has cooled down can cause hand burn.

Cause: Direct contact

Description:

Direct contact with crucible before the TGA has cooled down can lead to hand burn.

Likelihood of the incident (common to all consequence areas): **Unlikely (1)**

Kommentar:

It is highly unlikely that someone will touch the sample crucible before TGA has cooled down.

Consequence area: Helse

Assessed consequence: **Very large (4)**

Comment: Contact with crucible at 800 degree celcius can cause serious damage to skin. Adequate knowledge and proper handling of equipment must be employed.

Risk:





Hazard: Pressurized gas (air and/or inter gas)

Pressurized gas bottles of synthetic air or an inert gas are used in TGA experiment.

Incident: Gas leak

Improper installation of gas regulators may lead to gas leak.

Cause: Improper installation

Description:

Gas may leak through if the gas regulator is not installed properly.

Likelihood of the incident (common to all consequence areas): **Unlikely (1)**

Kommentar:

Hasn't happened while running any of my experiments however it happened with other people.

Consequence area: Helse

Assessed consequence: **Small (1)**

Comment: Synthetic air or an inert gas like Ar is not readily harmful.

Risk:


Consequence area: Materielle verdier

Assessed consequence: **Medium (2)**

Comment: Leakage of gas over time can be expensive, but the leakage can be detected in time using gas detectors.

Risk:





Hazard: Working in the lab under covid-situation

Working on Soxhlet extraction setup in Lab317 in the fumehood.

Incident: Contact with commonly used glass equipment

Glass equipments that are used by other users, such as round bottom flask, water bath, oil bath, thermometer, funnel, and beakers, may pose risk of infection, during covid-situation.

Likelihood of the incident (common to all consequence areas): **Less likely (2)**

Kommentar:

Likelihood of skin contact is quite low.

Consequence area: Helse

Assessed consequence: **Large (3)**

Comment: During covid19-situation, consequences may be severe.

Risk:



**Overview of risk mitigating measures which have been decided:**

Below is an overview of risk mitigating measures, which are intended to contribute towards minimizing the likelihood and/or consequence of incidents:

Overview of risk mitigating measures which have been decided, with description:



Detailed view of assessed risk for each hazard/incident before and after mitigating measures